1   **Holocene relative sea-level change along the tectonically active Chilean coast**

2

3   Ed Garrett[1]*, Daniel Melnick[2], Tina Dura[3], Marco Cisternas[4], Lisa L. Ely[5], Robert L. Wesson[6], Julius

4   Jara-Muñoz[7] and Pippa L. Whitehouse[8]

5

6   [1] Department of Environment and Geography, University of York, York, UK

7   [2] Instituto de Ciencias de la Tierra, TAQUACh, Universidad Austral de Chile, Valdivia, Chile

8   [3] Department of Geosciences, Virginia Tech, Blacksburg, VA, USA

9   [4] Instituto de Geografía, Pontificia Universidad Católica de Valparaíso, Valparaíso, Chile

10   [5] Department of Geological Sciences, Central Washington University, Ellensburg, WA, USA

11   [6] U.S. Geological Survey, Denver, CO, USA

12   [7] Department of Earth and Environmental Sciences, University of Potsdam, Potsdam, Germany

13   [8] Department of Geography, Durham University, Durham, UK

14

15   *Corresponding author: ed.garrett@york.ac.uk, Wentworth Way, Heslington, York, YO10 5NG,

16   United Kingdom

1

17   **Abstract**

18

19   We present a comprehensive relative sea-level (RSL) database for north, central, and south-central

20   Chile (18.5°S − 43.6°S) using a consistent, systematic, and internationally comparable approach.

21   Despite its latitudinal extent, this coastline has received little rigorous or systematic attention and

22   details of its RSL history remain largely unexplored. To address this knowledge gap, we re-evaluate

23   the geological context and age of previously published sea-level indicators, providing 78 index points

24   and 84 marine or terrestrial limiting points spanning from 11 ka to the present day. Many data

25   points were originally collected for research in other fields and have not previously been examined

26   for the information they provide on sea-level change. Additionally, we describe new sea-level data

27   from four sites located between the Gulf of Arauco and Valdivia. By compiling RSL histories for 11

28   different regions, we summarise current knowledge of Chilean RSL. These histories indicate mid

29   Holocene sea levels above present in all regions, but at highly contrasting elevations from ~30 m to

30   < 5 m. We compare the spatiotemporal distribution of sea-level data points with a suite of glacial

31   isostatic adjustment models and place first-order constraints on the influence of tectonic processes

32   over 10^3 to 10^4 year timescales. While seven regions indicate uplift rates < 1 m ka^{-1}, the remaining

33   regions may experience substantially higher rates. In addition to enabling discussion of the factors

34   driving sea-level change, our compilation provides a resource to assist attempts to understand the

35   distribution of archaeological, palaeoclimatic, and palaeoseismic evidence in the coastal zone and

36   highlights directions for future sea-level research in Chile.

37

38   Keywords: Holocene; Sea-level changes; South America; Data analysis; Sea-level database; Glacial

39   isostatic adjustment; Tectonics

2

1. Introduction

Eustatic, isostatic, tectonic, and local factors drive changes in Holocene relative sea level (RSL) (Farrell and Clark, 1976; Pirazzoli, 1991). Compilations of regional databases of Holocene index points, which constrain the age and elevation of past sea level, advance our understanding of the mechanisms and relative contributions of these driving factors in time and space. They highlight regional differences, provide constraints on glacial isostatic adjustment models and serve as a baseline for assessing future sea-level changes (Shennan et al., 2012, 2018; Engelhart et al., 2015; Khan et al., 2015; Vacchi et al., 2016). Despite extending through more than 37° of latitude, the Chilean coastline has not previously received rigorous or systematic attention, and details of its RSL history remain poorly understood. While previous coastal zone investigations have focussed on archaeology (e.g. Pino and Navarro, 2005; May et al., 2015), palaeoseismology (e.g. Cisternas et al., 2005; 2017; Dura et al., 2015; 2017; Garrett et al., 2015), tectonics (e.g. Stefer et al., 2010; Melnick et al., 2019), and palaeoclimate (e.g. Villa-Martínez and Villagrán, 1997; Frugone-Álvarez et al., 2017), only a limited number of studies have specifically addressed Holocene sea-level evolution (e.g. Leonard and Wehmiller, 1991; Atwater et al., 1992; Nelson and Manley, 1992). The limited scope of previous Holocene sea-level data compilations (Isla, 1989; Isla et al., 2012) and the potential to increase the temporal and spatial resolution of RSL histories in Chile using data from other fields of study necessitates a reappraisal of RSL data from this region.

For the first time, this paper compiles a comprehensive sea-level database for north, central, and south-central Chile (18.5°S – 43.6°S; Fig. 1) using a consistent, systematic, and internationally comparable approach (Hijma et al., 2015; Khan et al., 2019). Our database incorporates a range of different types of sea-level indicators, including tidal marsh sediments, beach ridges, marine deposits and freshwater sediments, dated using radiocarbon and luminescence approaches. We re-evaluate the geological context and age of previously published sea-level data, providing 78 index

points (reconstructions of the elevation of RSL at a specific time and location) and 84 limiting points (which place minimum or maximum constraints on the elevation of RSL) that span the period from 11000 years ago to the present day. We also present a new index point and three new limiting points from four sites between 35.8°S and 43.6°S. By compiling and comparing the RSL history for 11 different regions, we seek to summarise current knowledge of Chilean RSL, highlight directions for future sea-level research, and provide a resource to assist research into archaeological, palaeoclimatic, and palaeoseismic records in the coastal zone.
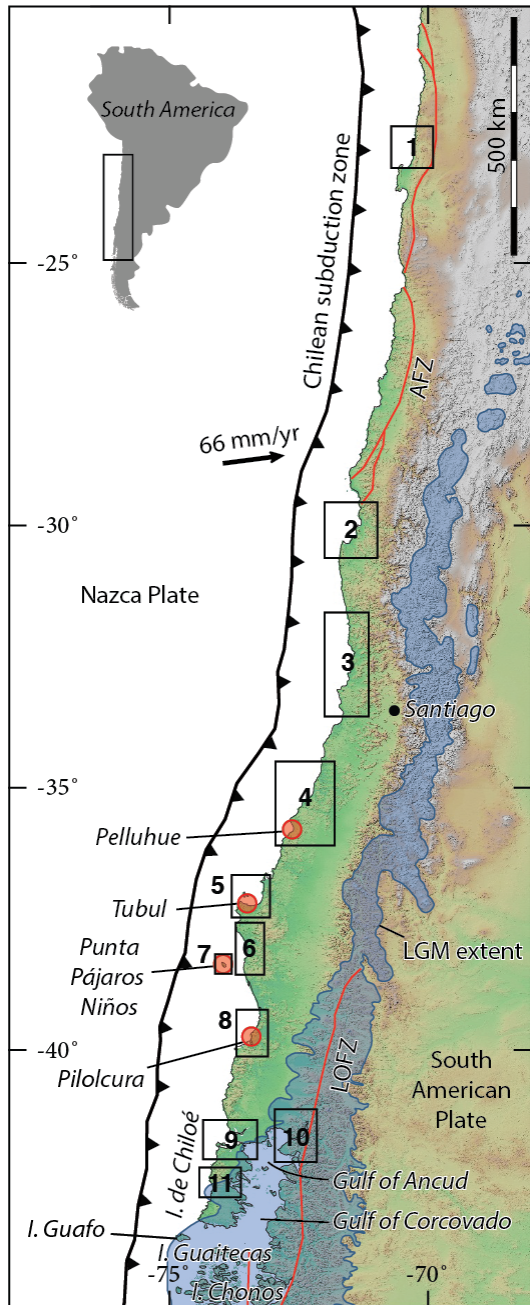
Figure 1: Location of the sea-level data points assessed in this study, grouped into regions (black boxes). Red circles indicate new sites reported here for the first time. AFZ: Atacama fault zone, LOFZ: Liquiñe-Ofqui fault zone, LGM: Last Glacial Maximum extent of the Patagonian ice sheet (blue shading, following Ehlers et al., 2011).

2. Study area

82   We restrict our review of published sea-level data to the coastline between Arica (18.5°S) and Isla

83   Guafo (43.6°S), a straight-line distance of almost 3000 km (Fig. 1). This coastline possesses a

84   consistent tectonic setting, characterised by subduction of the Nazca Plate beneath South America.

85   Despite the continuity in tectonic setting between Isla Guafo and the triple junction, close to the

86   Taitao Peninsula (46.5°S), we do not discuss sites in this region due to the complex tidal regimes

87   associated with the fjord setting. Due to its remote nature, few published Holocene sea-level records

88   currently exist between Isla Guafo and the Taitao Peninsula; however, we note that Reyes et al.

89   (2018) discuss coastal archaeological sites from the Guaitecas (43.9°S) and Chonos (45.3°S)

90   archipelagos and provide minimum ages for the marine terraces on which these sites are located.

91   While increased tidal ranges also influence sites bordering the gulfs of Ancud and Corcovado on the

92   western side of Isla de Chiloé (Fig. 1), we include the small number of data points available from this

93   area due to their proximity to sites facing the open ocean. Sea-level data are available from the

94   southernmost regions of Chile (e.g. Porter et al., 1984; Rabassa et al., 1986; Gordillo et al., 1992;

95   McCulloch and Davies, 2001; Bentley and McCulloch, 2005); however, the unique glacial history of

96   this region, the different tectonic setting, and the importance of local postglacial faulting mean they

97   deserve a separate analysis and lie beyond the scope of this paper.

98

99   2.1 Tectonic setting

100

101 In contrast to the largely stable locations on which the majority of previous sea-level databases

102 focus, Chilean RSL change is influenced by significant tectonic activity associated with the subduction

103 of the Nazca Plate. Plate convergence induces both folding and faulting within the overriding South

104 American Plate and deformation associated with megathrust earthquakes on the subduction

105 interface (Barrientos, 2007). Since the start of the 20th century, at least eight Chilean earthquakes

106 have exceeded magnitude (M_w) 8, including the largest event since the inception of modern seismic

107 recording, the 1960 CE M_w 9.5 Valdivia earthquake and the 2010 CE M_w 8.8 Maule earthquake.

108   Decimetre- to metre-scale coseismic land-surface deformation accompanies these great

109   earthquakes, resulting in abrupt relative sea-level changes over hundreds to thousands of kilometres

110   of coastline (Plafker and Savage, 1970; Farías et al., 2010; Dura et al., 2017). Major interplate

111   earthquakes (magnitude 7 – 8), occurring along the margin at a rate of ~50 per century, may also

112   result in decimetre-scale land-surface deformation along tens of kilometres of coastline (Xu, 2017;

113   Garrett et al., 2019). The sea-level history of tectonically active regions reflects these vertical

114   coseismic changes and also the slower postseismic and interseismic deformation associated with

115   strain accumulation between earthquakes.

116

117   In addition to deformation associated with slip on the subduction interface, concurrent splay faulting

118   within the upper plate may contribute to abrupt local decimetre- to metre-scale changes in relative

119   sea level (Melnick et al., 2012; Jara-Muñoz et al., 2017). Upper plate faults may also rupture quasi-

120   independently of the megathrust. Two major fault systems lie parallel to the convergent margin (Fig.

121   1): the Atacama fault zone of the northern coastal cordillera and the Liquiñe-Ofqui fault zone, a

122   dextral intra-arc transform fault of the main cordillera of south-central and southern Chile

123   (Cembrano *et al*., 1996; Rosenau et al., 2006; Rehak *et al*., 2008). Instrumentally recorded

124   earthquakes associated with these structures have not exceeded M_w 6.2 or produced evident

125   coseismic coastal deformation (Barrientos, 2007; Lange et al., 2008).

126

127   2.2 Glacial history

128

129   At the maximum extent of the last glacial period, the Patagonian ice sheet extended along the Andes

130   from ~38°S to ~56°S (Caldenius, 1932; Denton et al., 1999; Hulton et al., 2002; Glasser et al., 2008).

131   The distribution of moraines and outwash plains suggests a piedmont lobe extended from the

132   mainland and overran the southern half of Isla de Chiloé (Fig. 1), while northern Isla de Chiloé and

133   the coastline of the mainland to the north remained ice free (Heusser and Flint, 1977; García, 2012).

7

134   In the south, the Patagonian ice sheet covered the Chilean mainland and outlying islands, with a

135   modelled volume equivalent to 1.2 m of global sea level (Hulton et al., 2002). Patagonian piedmont

136   glaciers rapidly retreated after 17500 – 17150 a BP (Denton et al., 1999; McCulloch et al., 2000), with

137   the ice sheet losing over 80 % of its Last Glacial Maximum volume within 2000 years (Hulton et al.,

138   2002). Relative warmth characterised the period from 13500 to 4000 a BP (Heusser and Streeter,

139   1980; Rabassa and Clapperton, 1990), before late Holocene cooling and increases in precipitation

140   resulted in Neoglacial icefield expansion (Glasser at al., 2004; Bertrand et al., 2012). Three or four

141   periods of glacier advance ensued, including during the Little Ice Age (Mercer, 1970; Aniya, 1996;

142   Araneda et al., 2007). Subsequent retreat has reduced the combined contemporary extent of the

143   North and South Patagonian icefields (47°S – 51°S) and the smaller, discontinuous icefields of the

144   Cordillera Darwin (54°S – 55°S) to 17,000 km^2 (Rignot *et al*., 2003). The contribution of the two larger

145   icefields to global sea-level rise has averaged 0.0052 ± 0.0008 mm yr^{-1} since 1870 (Glasser et al.,

146   2011). This figure has increased to 0.067 ± 0.004 mm yr^{-1} between 2000 and 2012 (Willis et al.,

147   2012).

148

149   **3. Database methodology**

150

151   Through a series of International Geological Correlation Programme and International Geoscience

152   Programme (IGCP) projects (numbers 61, 200, 274, 367, 437, 495, 588 and 639), the sea-level

153   community has derived and implemented standardised and globally applicable approaches to sea-

154   level reconstruction. Integral to this endeavour, sea-level databases synthesise data from different

155   studies to reconstruct regional relative sea-level histories (Bloom, 1977; Pirazzoli, 1991; Shennan et

156   al., 2002; Khan et al., 2019). Databases contain sea-level index points, reconstructions of the

157   elevation of RSL at a specific time and location, and limiting points, which place minimum or

158   maximum constraints on the elevation of RSL (marine and terrestrial limiting points respectively).

159   Our database compiles sea-level indicators from the literature, interpreting data from a wide range

8

160   of sources as either index or limiting points. For each data point, we quantify sources of vertical and

161   temporal uncertainty following the approach set out by Hijma et al. (2015).

162

163   We subdivide our database into 11 regions based primarily on the proximity and clustering of sites.

164   We assign sites to regions minimising the distances between sites within a region and maximising

165   the distances between regions. The mean distance between a site and the centroid of its respective

166   region is 22 km, with the centroids of adjacent regions generally separated by > 100 km. Despite the

167   shorter distance between sites on Isla Mocha (region 7) and the adjacent mainland (region 6), we

168   separate these regions based on their different tectonic histories (Nelson and Manley, 1992).

169   Further subdivision to a finer spatial scale is currently unwarranted due to the low total number of

170   sites and data points.

171

172   3.1 Data sources

173

174   Few studies have explicitly focussed on the history of RSL change in Chile; consequently, our data are

175   principally derived from coastal investigations with different foci. In central and south-central Chile,

176   we reanalyse sea-level indicators resulting from investigations into the occurrence of Holocene

177   subduction zone earthquakes and tsunamis (e.g. Atwater et al., 1992; Cisternas et al., 2005; Nelson

178   et al., 2009; Ely et al., 2014; Dura et al., 2015; Garrett et al., 2015; Hong et al., 2017). We also obtain

179   sea-level data from datasets previously used to constrain tectonic uplift rates (Stefer et al., 2010;

180   Melnick et al., 2019), identify human occupation of the coastal zone (Pino and Navarro, 2005), and

181   reconstruct palaeoclimatic change (Villa-Martínez and Villagrán, 1997; Frugone-Álvarez et al., 2017).

182   In northern and north-central Chile, we incorporate sea-level data from studies that have sought to

183   constrain the age and elevation of mid-Holocene RSL (e.g. Ota and Paskoff, 1993; May et al., 2013;

184   Hart et al., 2017). Similar RSL-focussed investigations in central and south-central Chile are less

185   numerous (e.g. Nelson and Manley, 1992; Isla et al., 2012). Previous compilations included just three

9

186 (Isla, 1989) and ~30 (Isla et al., 2012) sea-level data points from our regions of interest. The use of a

187 wider range of data sources provides a substantially expanded compilation and, for the first time,

188 our compilation incorporates comprehensive data quality control and error assessment.

189

190 3.2 Indicative meaning

191

192 To serve as an index point, a sea-level indicator must have a defined relationship with tidal levels, or

193 *indicative meaning* (van de Plassche, 1986; Shennan, 2015). The indicative meaning consists of the

194 *reference water level*, the elevation at which the indicator occurs with respect to contemporaneous

195 tidal levels, and the *indicative range*, the span of elevations at which the indicator might be found.

196 We define indicative ranges for seven different types of index points and define reference water

197 levels as the mid-points of the indicative ranges (Table 1). We obtain tidal datums for each location,

198 modelling mean lower low water (MLLW), mean low water (MLW), mean tide level (MTL), mean high

199 water (MHW), mean higher high water (MHHW), and highest astronomical tide (HAT) using the

200 TPXO8-ATLAS global model of ocean tides (Egbert and Erofeeva, 2010). We scale the modelled tidal

201 amplitude for each location following analysis of the differences between the tidal model and data

202 from 21 permanent tide gauge stations (supplementary information S1).

203

204 Table 1: Definition of the indicative meaning of the different sea-level indicators assessed in this

205 study. The reference water level is defined as the midpoint of the indicative range. HAT: Highest

206 Astronomical Tide, MHHW: Mean Higher High Water; MHW: Mean High Water, MTL: Mean Tide

207 Level, MLLW: Mean Lower Low Water.

Sample type	Evidence	Reference water level	Indicative range
Index points			
High tidal marsh environment	Organic sediments. High marsh plant macrofossils. Diatom or foraminiferal assemblages dominated by high marsh taxa.	(MHW+HAT)/2	MHW – HAT
Low tidal marsh/upper tidal flat environment	Organic or clastic sediments. Low marsh plant macrofossils. Diatom or foraminiferal assemblages dominated by low marsh/upper tidal flat taxa.	(MTL+MHW)/2	MTL – MHW

Undifferentiated tidal marsh environment	Organic sediments. Microfossil and macrofossil assemblages dominated by tidal marsh taxa that do not meet the requirements to be classified as strictly low or high tidal marsh.	(MTL+HAT)/2	MTL – HAT
Specified tidal marsh environment	Estimate of RWL and IR from quantitative approach e.g. microfossil transfer function.	Uniquely defined	Uniquely defined
Undifferentiated intertidal environment	Clastic sediments. Microfossils a mix of marine, brackish and freshwater species. May be supported by geomorphic setting.	(MLLW+HAT)/2	MLLW – HAT
Beach ridges	Sand- or gravel-rich shore-parallel ridges with a gently dipping or horizontal landward surface and a more steeply dipping seaward face.	HAT+1.5 m	HAT – HAT+3m
Undifferentiated beach environment	Sand- or gravel-rich sediments, may contain shells or shell fragments. Includes beachface, berm and beach ridge environments.	(MLLW – HAT+3m)/2	MLLW – HAT+3m
Limiting points			
Marine sediments	Clastic sediments containing marine diatom or foraminiferal assemblages or in-situ marine shells.	MTL	Below MTL
	Clastic sediments without (or without reported) identifiable macrofossils or microfossils.	MHHW	Below MHHW
	Coquina containing transported intertidal or subtidal molluscs but lacking morphology indicative of supratidal beach ridge deposition.	HAT	Below HAT
	Undifferentiated clastic sediments where neither beach ridge nor subtidal deposition can be discounted	HAT+3m	Below HAT+3m
Terrestrial sediments	Organic soil or peat with freshwater microfossil assemblages or in-situ freshwater plant macrofossils (e.g. tree stumps).	HAT	Above HAT
	Organic soil or peat without (or without reported) identifiable intertidal macrofossils or microfossils.	MTL	Above MTL
	Organic or clastic sediments with sedimentary structures, faunal or floral assemblages, or geochemical composition typical of lacustrine sedimentation.	HAT	Above HAT
	Clastic sediments exhibiting sedimentary structures typical of aeolian dunes.	HAT	Above HAT
	Clastic sediments exhibiting sedimentary structures typical of colluvial wedges.	HAT	Above HAT

208

209 Tidal marsh environments provide the majority of our index points. We separate these into low

210 marsh, high marsh, undifferentiated marsh, and specified marsh environments based on macro- and

211 microfossil evidence (Atwater et al., 1992; Nelson et al., 2009; Garrett et al., 2015). Specified tidal

212 marsh refers to samples with indicative meanings provided in the original study by the statistical

213 comparison of modern and fossil microfossil assemblages, usually diatoms, using transfer functions

214 (e.g. Garrett et al., 2015). The second largest group of index points come from beach ridges and

215 undifferentiated beach environments. The relationship between the elevation of a beach ridge crest

216   and coeval sea level is complex, with elevation reflecting wave run-up and other sediment transport

217   mechanisms (Orford et al., 1991; Otvos, 2000; Tamura, 2012). Tamura (2012) recommends that

218   sandy beach ridges are not used as sea-level indicators as the uncertainties involved are frequently

219   too large in comparison with reconstructed sea-level changes since the mid Holocene. As we are not

220   seeking to identify small-scale sea-level changes, we choose to incorporate sandy beach ridges and

221   account for uncertainties using appropriately cautious indicative ranges. Furthermore, the presence

222   of low elevation modern ridges and the occurrence of multiple fossil ridges at low elevations

223   indicates Chilean beach ridges form within a few metres of contemporaneous sea level (Nelson and

224   Manley, 1992; Bookhagen et al., 2006). On the Atlantic coast of Patagonia, Schellmann and Radtke

225   (2010) suggest that beach ridge crests lie between 2 and 3 m above the highest tide level on exposed

226   shorelines and down to 1 m or less above the highest tides in wave-protected areas. In this work, we

227   conservatively consider beach ridge crests to lie between HAT and 3 m above HAT (Table 1). Where

228   sediments are described by the original authors as "beach deposits" or similar, we extend the

229   indicative range described above for beach ridges to include the intertidal zone (i.e. between MLLW

230   and HAT + 3m). A similar approach was recently used by Vacchi et al. (2018) in eastern Canada.

231

232   Terrestrial and marine limiting points each have a reference water level, but as their precise

233   relationship with contemporaneous sea level is unknown, their indicative ranges are simply open-

234   ended windows above or below the reference water level (Table 1). Marine limiting points include

235   clastic sediments containing in situ marine macro- or microfossils, coquinas (deposits largely

236   consisting of reworked shells), and clastic sediments without (or without reported) fossils. Terrestrial

237   limiting points include freshwater marshes, lake sediments, and aeolian dunes. We use above MTL

238   as a conservative indicative range, unless unequivocal evidence (e.g. in situ tree roots) warrants the

239   use of HAT as the reference water level (Table 1).

240

241   3.3 Quantifying vertical uncertainties

       12

242

243 We account for errors in the vertical position of each sea-level indicator, considering uncertainties in

244 the sample depth and the absolute elevation of the top of the core, pit or exposure. Where these

245 uncertainties are not explicitly stated by the original authors, we estimate appropriate values

246 following Hijma et al. (2015). Where elevations are related to "mean sea level" (including datums of

247 uncertain meaning such as "sea level", "modern sea level") or other tidal levels, and lack further

248 details of how they were derived, we define the corresponding tidal uncertainty as ± 0.5 m, in

249 keeping with the magnitude of uncertainties proposed by Hijma et al. (2015) for elevations derived

250 from vegetation zones, digital elevation models, or using water depth measurements. Where sample

251 elevations are relative to tidal levels measured using a portable tide gauge, with measurements over

252 hours or days, we estimate the corresponding uncertainty as ± 0.07 m following Wesson et al.

253 (2014). In the absence of local conversions from a reference geoid to mean sea level, where

254 elevations are given with respect to the EGM96 geoid, we do not account for differences between

255 this model and MSL. We do, however, include a vertical error of ± 0.20 m to reflect the uncertainty

256 of this conversion (or lack thereof), reflecting the magnitude of the offsets identified for the Gulf of

257 Arauco by González-Acuña (2012). We note that the future application of geoid undulation models

258 may change the elevation of a small number of index and limiting points.

259

260 To account for disparities between the tidal model—which does not incorporate atmospheric

261 effects—and actual tides, we include a further vertical uncertainty associated with modelling each

262 reference water level based on a comparison of model predictions and data from 21 permanent tide

263 gauges (supplementary information S1). This uncertainty is calculated as a percentage of the

264 modelled reference water level and is site and sample-type specific, ranging from <0.01 m to 0.27 m.

265

266 3.4 Accounting for tectonics, compaction and tidal range changes

267

13

268   For sites within the rupture zone of the 2010 Maule earthquake, where elevations were determined

269   before 2010, we adjust for coseismic deformation using estimates of uplift or subsidence, with

270   corresponding errors, from published field data (Farías et al., 2010; Melnick et al., 2012). Due to a

271   lack of data, we do not adjust for postseismic deformation following the 2010 earthquake. Similarly,

272   for sites outside the 2010 rupture area, we do not account for changes in RSL caused by interseismic

273   deformation or other processes occurring between the timing of data collection and the present

274   day. We do not correct for millennial-scale tectonic motions before presenting regional sea-level

275   histories; rather, we choose to discuss reconstructed relative sea-level changes with respect to

276   driving factors including tectonics.

277

278   The majority of Chilean index and limiting points come from intercalated rather than basal settings

279   and may be influenced by compaction. Intense seismic shaking could potentially exacerbate this

280   phenomenon. Sediment compaction after deposition lowers intercalated sedimentary sea-level

281   indicators, but does not influence basal data points (Horton and Shennan, 2009; Brain et al., 2012).

282   Noting a lack of work on compaction in South American marshes and the scarcity of information on

283   the depth to consolidated strata for many sea-level indicators in the database, we do not attempt to

284   apply a correction for this factor.

285

286   Due to the predominantly linear and open configuration of the Chilean coast, we anticipate that

287   latitudinal variations in tidal range are likely to have been consistent over the Holocene. Sites

288   fringing the semi-enclosed gulfs on the eastern side of Isla de Chiloé are more likely to have

289   experienced changes in tidal range; however, with the small number of data points from this region

290   and without further information available on palaeotidal ranges, we do not consider this process in

291   the current compilation.

292

293   3.5 Chronological control

14

294

295   Radiocarbon and luminescence approaches provide ages for each of the sea-level indicators. Where

296   publications use radiocarbon dating, we recalibrate all ages using OxCal v.4.2 (Bronk Ramsey, 2009)

297   and the latest calibration curves: ShCal13 (Hogg et al., 2013), Marine13 (Reimer et al., 2013), and

298   Bomb13: southern hemisphere zone (Hua et al., 2013). An offset from the global marine reservoir

299   (ΔR) must be applied where radiocarbon dates relate to marine samples; however, the Chilean

300   coastline is poorly represented in the global marine reservoir database (http://calib.org/marine/).

301   Two samples from Valparaíso (33°S) provide contrasting offsets of 61 ± 50 years (Ingram and

302   Southon, 1996) and 313 ± 76 years (Taylor and Berger, 1967). To reflect this uncertainty, we use the

303   weighted average of these samples, 137 ± 164 years, as the offset for all locations south of 28.5°S.

304   Towards the northern limit of the region discussed here, Taylor and Berger (1967) report an offset of

305   175 ± 34 years from Antofagasta (24°S). Ortlieb et al. (2011) report temporally variable ΔR values

306   from between 14°S and 24°S. We employ their mid to late Holocene mean value of 226 ± 98 years as

307   the offset for the single site included in our database that lies north of 28.5°S.

308

309   3.6 Data visualisation

310

311   On figures summarising the age and elevation of sea-level data points, we plot sea-level index points

312   as rectangles, with the height proportional to the vertical uncertainty in RSL and the width

313   proportional to the 2σ age range. Following Hijma et al. (2015), we plot terrestrial limiting dates as

314   green T-shaped symbols and marine limiting dates as blue ⊥-shaped symbols. An arrowhead at the

315   end of the vertical line points towards RSL lying below (for T-shaped terrestrial limiting points) or

316   above (for ⊥-shaped marine limiting points) the horizontal line, which sits at the extreme limit of the

317   uncertainty range. The length of the vertical line reflects the total vertical uncertainty. We note that

318   some studies have inverted the use of these symbols (Vacchi et al., 2016; Khan et al., 2017; García-

319 Artola et al., 2018), although not the colours, and care must consequently be taken to ensure that

320 the intended meaning is fully understood.

321

322 3.7 Modelling glacial isostatic adjustment and tectonic uplift

323

324 To investigate the processes driving RSL change, we compare sea-level data with glacial isostatic

325 adjustment (GIA) models. A GIA model requires two inputs: information about past global ice sheet

326 change (the 'ice model') and information about the rheological properties of the solid Earth (the

327 'Earth model'). For the purposes of this study, we assume Earth structure varies only radially,

328 enabling us to define a series of 'one-dimensional' Earth models that differ in terms of the values

329 assumed for lithospheric thickness and upper/lower mantle viscosity. For each of the 11 regions, we

330 predict RSL at the centre of each region at 1 ka intervals using two ice models, ICE-5G (Peltier, 2004)

331 and ICE-6G (Peltier et al., 2015). Each ice model is combined with 12 one-dimensional Earth models

332 that encompass a realistic range of rheologies for the subduction zone. We use lithospheric

333 thicknesses of 71, 96 and 120 km and upper mantle viscosities of 5×10^{19} Pa s, 8×10^{19} Pa s, 1×10^{20}

334 Pa s, and 2×10^{20} Pa s, with a lower mantle viscosity of 10^{22} Pa s. Our upper mantle viscosities are

335 lower than those typically used in passive margin settings (e.g. Shennan et al., 2018; Vacchi et al.,

336 2016) and in previous studies of coastal palaeoseismic evidence (Dura et al., 2016). As such, they

337 more closely reflect rheologies inferred at seismic-cycle timescales in Chile (Khazaradze et al., 2002;

338 Lorenzo-Martin et al., 2006; Li et al., 2018) and other subduction zones (e.g. Wiseman et al., 2015;

339 Freed et al., 2017). Studies of crustal rebound following recent ice loss from the Patagonian Icefields

340 similarly suggest low upper mantle viscosities (Lange et al., 2014; Richter et al., 2016).

341

342 To assess the possible role and rates of millennial-scale tectonic uplift, we apply a range of linear

343 corrections to the RSL data to improve the fit with the GIA model predictions in each region. To

344 allow for shorter-term variability resulting from centennial-scale earthquake deformation cycles, we

16

345   include a ± 1 m envelope around the model predictions. The magnitude of this envelope provides a

346   conservative assessment of centennial cycles, reflecting the upper bound of vertical deformation

347   recorded at coastal sites during 20th and 21st century great earthquakes (Plafker and Savage, 1970;

348   Farías et al., 2010; Klein et al., 2017). We accept all corrections that result in index points (including

349   error terms) overlapping the suite of model predictions, terrestrial limiting points sitting within or

350   above the predictions, and marine limiting points lying within or below the predictions.

351

352   **4. New sea-level data**

353

354   In addition to compiling and standardising sea-level data from the literature (section 5), we present

355   four new sea-level data points from hitherto unstudied sites.

356

357   4.1 Pelluhue, Maule region

358

359   At Pelluhue (35.8133°S 72.5762°W), an outcrop at the landward edge of the contemporary beach

360   exposes an abrasion platform carved into metamorphic bedrock. Black volcanic sand and a colluvial

361   wedge overlie the platform (Fig. 2). The medium to coarse volcanic sand is similar in composition

362   and grain size to the contemporary beach sand but lacks datable organic material. The colluvium

363   consists of angular pebbles, rounded cobbles and charcoal fragments that we interpret as having

364   accumulated above the reach of tides. We radiocarbon dated three charcoal fragments from a layer

365   at the base of the colluvium at an elevation of 4.87 ± 0.15 m MSL. The resulting dates constrain the

366   timing of the deposition of the colluvium; the median calibrated ages lie within 100 years of each

367   other (Table 2). The youngest calibrated age range, 4407 – 4095 cal a BP, provides the age for a

368   terrestrial limiting point. We derive the maximum elevation of RSL by taking the reference water

369   level (HAT = 1.08 m) away from the sample elevation and adding the sum of the positive vertical

370   uncertainties (comprising uncertainties related to the absolute elevation, the depth within the

17

371   section, and the indicative meaning: 0.19 m). The terrestrial limiting point therefore indicates RSL

372   was below 3.98 m.

373
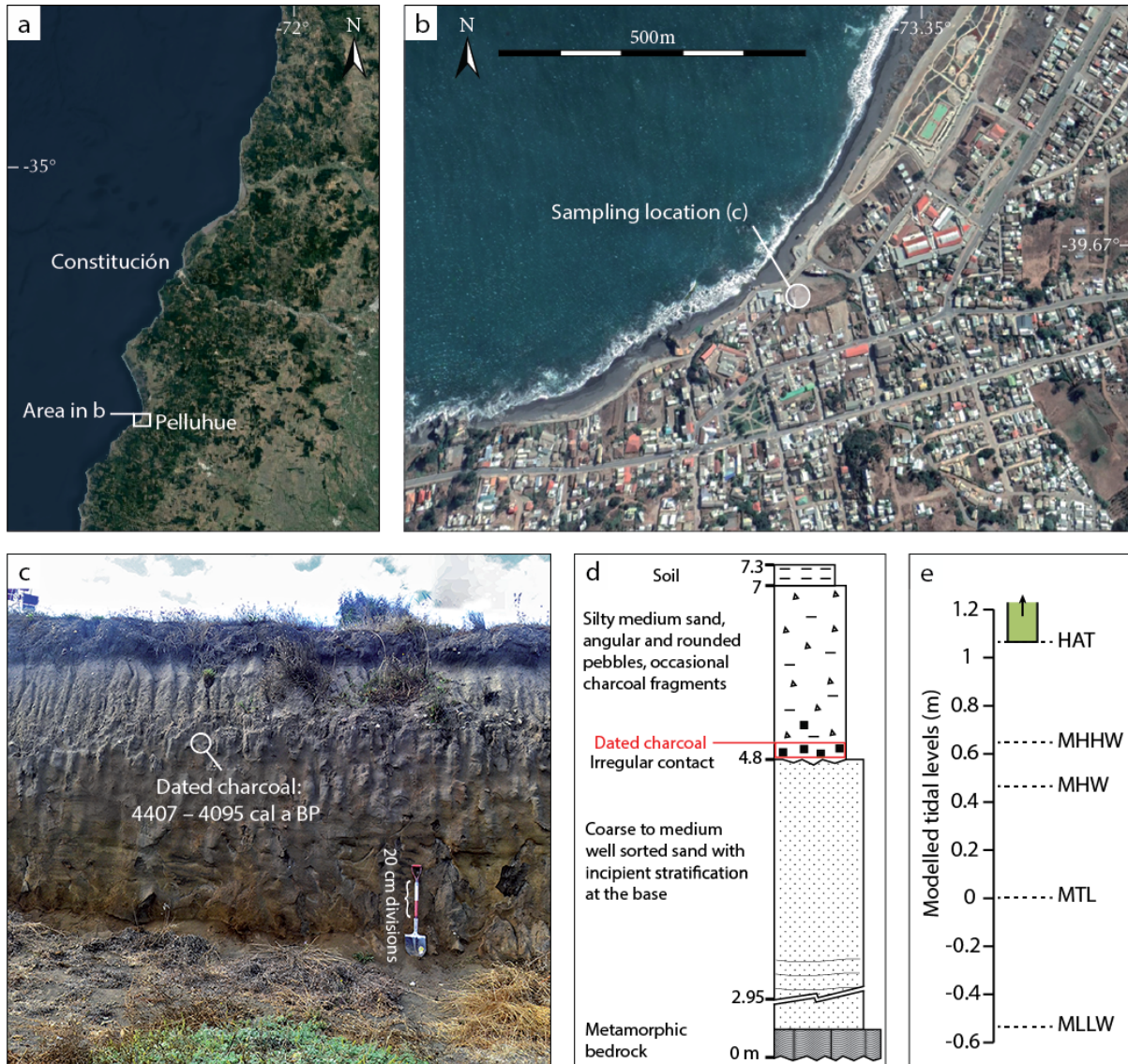
374

375   Figure 2: Derivation of the new terrestrial limiting point from Pelluhue. a) Location of Pelluhue and

376   b) sampling location. c) Photograph and d) stratigraphic log of the dated section. e) Graphical

377   representation of the terrestrial limiting point's indicative meaning (open-ended green box; above

378   highest astronomical tide) relative to tidal levels at the site modelled using the TPXO8-ATLAS tidal

379   model (Egbert and Erofeeva, 2010). Basemaps in a) and b) are from Bing Maps.

380

18

381 Table 2: Radiocarbon data associated with the new sea-level data points from Pelluhue, Tubul, Punta

382 Pájaros Niños, and Pilolcura. Reported ages are conventional ^{14}C ages in years before 1950 CE,

383 corrected for isotopic fractionation using δ^{13}C (NR = δ^{13}C not reported). Ages calibrated with OxCal

384 4.2 (Bronk Ramsey, 2009) and the SHCal13 calibration curve (Hogg et al., 2013), except for the

385 calibrated range marked *, which are calibrated using the Marine13 calibration curve (Reimer et al.,

386 2013) and ΔR = 137 ± 164 years, as discussed in section 3.5.

387

Sample name	Laboratory code	Sample elevation (mMSL)	Dated material	δ^{13}C	[14]C years BP ± 1σ	Calibrated age (years BP, 2σ)
Pelluhue						
PEL001	Poz-50368	4.87 ± 0.15	Charcoal fragment	-23.8	3925 ± 35	4420 – 4158
PEL002	Poz-50369	4.87 ± 0.15	Charcoal fragment	-25.5	3890 ± 35	4412 – 4150
PEL003	Poz-50370	4.87 ± 0.15	Charcoal fragment	-25.0	3870 ± 35	4407 – 4095
Tubul						
TUB001	Beta-276181	2.72 ± 0.13	*Petricola rugosa* shell	-0.5	4780 ± 40	5302 – 4421*
Punta Pájaros Niños, Isla Mocha						
PPN001	KIA 36874	21.9 ± 0.20	*Leukoma thaca* shell	-1.1	3625 ± 30	3790 – 2934*
Pilolcura						
PIL001	D-AMS 032803	2.47 ± 0.07	Charcoal fragment	NR	1161 ± 36	1089 – 932

388

389 4.2 Tubul, Arauco region

390

391 One kilometre north of the mouth of the Río Tubul (37.2265°S 73.4357°W), a partially exhumed

392 wave-cut bedrock platform, cut into siltstone from the Plio-Pleistocene Tubul Formation, lies above

393 present sea level (Fig. 3). The surface of the platform is heavily pitted by the subtidal to low

394 intertidal rock-boring bivalves *Petricola rugosa*, *Petricola dactylus* and *Pholas chiloensis.* A poorly

395 consolidated clast-supported conglomerate containing subrounded bivalve-bored mudstone and

396 sandstone cobbles and boulders, gravel, articulated and fragmented subtidal clams (*Leukoma thaca*),

397 marine gastropods (*Turitella* sp.), charcoal fragments, and a sand-rich matrix locally overlies the

398 platform. We hypothesise that this conglomerate results from the debris from a landslide from the

399 adjacent cliffs that was subsequently reworked by waves. We base this assumption on our

400 observations of similar effects seen after the 2010 earthquake, which triggered a landslide above the

19

401   studied site. Since 2010, we have observed how storm waves have reworked the resulting landslide

402   debris.

403

404   We dated an articulated *Petricola rugosa* shell found in life position inside its hole in the bedrock

405   platform, which was preserved beneath the conglomerate (Table 2). As living *P. rugosa* individuals

406   are found beneath MTL and generally in water depths of less than 10 m (Bernard, 1983), the

407   resulting calibrated date, 5302 – 4421 cal a BP, provides the age of a marine limiting point.

408   Accounting for the sample elevation (2.69 m), the reference water level (MTL = -0.01 m), and the

409   sum of the negative vertical uncertainties (0.13 m), the limiting point indicates RSL above 2.57 m.
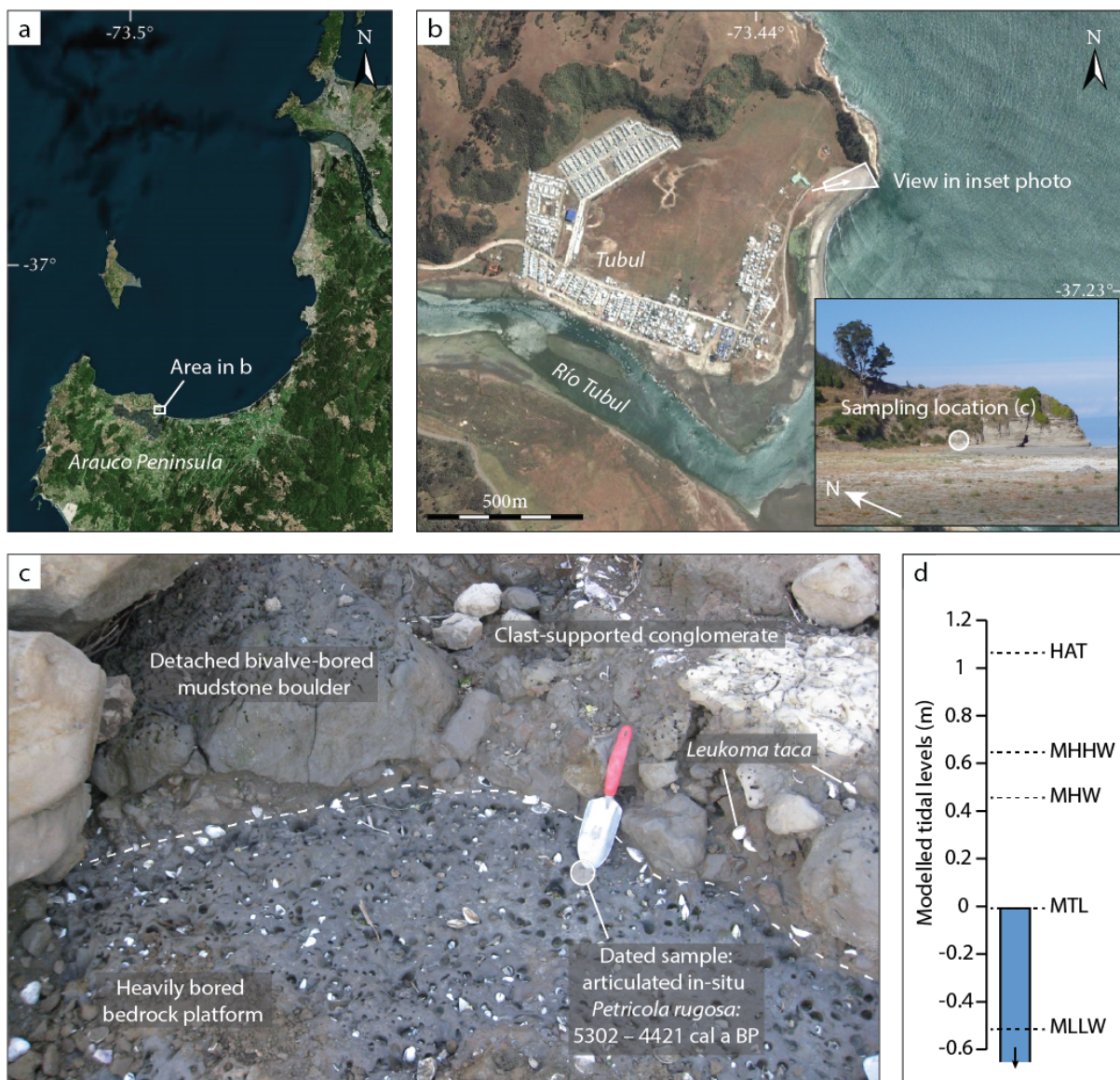

410

411   Figure 3: Derivation of the new marine limiting point from Tubul. a) Location of Tubul on the

412   northern side of the Arauco Peninsula, b) sampling location on the headland east of Tubul, c)

413   photograph of the bivalve-bored bedrock platform with the location of the dated *Petricola rugosa*, d)

414   graphical representation of the marine limiting point's indicative meaning (open-ended blue box;

415   below mean tide level) relative to tidal levels at the site modelled using the TPXO8-ATLAS tidal

416   model (Egbert and Erofeeva, 2010). Basemaps in a) and b) are from Bing Maps.

417

418   4.3 Punta Pájaros Niños, Isla Mocha

419

420   Towards the northernmost point of Isla Mocha, at Punta Pájaros Niños (38.3250°S 73.9549°W), we

421   encountered a coquina layer at an elevation of ~22 m (Fig. 4). The coquina contains bivalves

422   (*Leukoma thaca*) and gastropods (*Tegula atra* or *Diloma nigerrimum*), with a poorly cemented sandy

423   matrix. The high proportion of shell material and the presence of multiple marine species of differing

424   environmental preference, including subtidal species from sandy substrates and intertidal species

425   from rocky substrates, suggests reworking and deposition in a high-energy subtidal or possibly

426   intertidal environment. The layer lacks any morphological evidence for supratidal deposition in the

427   form of a beach ridge or shell midden, while the low gradient of the site substantially reduces the

428   possibility of post-depositional reworking. The thin overlying conglomerate is of fluvial origin, with

429   very well-rounded andesite clasts implying connectivity with the mainland or possibly reworking

430   from higher elevations, although the latter hypothesis appears less likely given the site morphology.

431   A whole, although not articulated, *Leukoma thaca* shell provides an age for the coquina of 3790 –

432   2934 cal a BP (Table 2). As the water depth at which coquina deposits form is unknown in this

433   setting, we conservatively treat the sample as a marine limiting point with an indicative range of

434   below HAT. Taking away the reference water level (HAT = 1.09 m) and the sum of the negative

435   vertical uncertainties (0.24 m) from the sample elevation (21.90 m) indicates RSL was above

436   20.57 m.

21
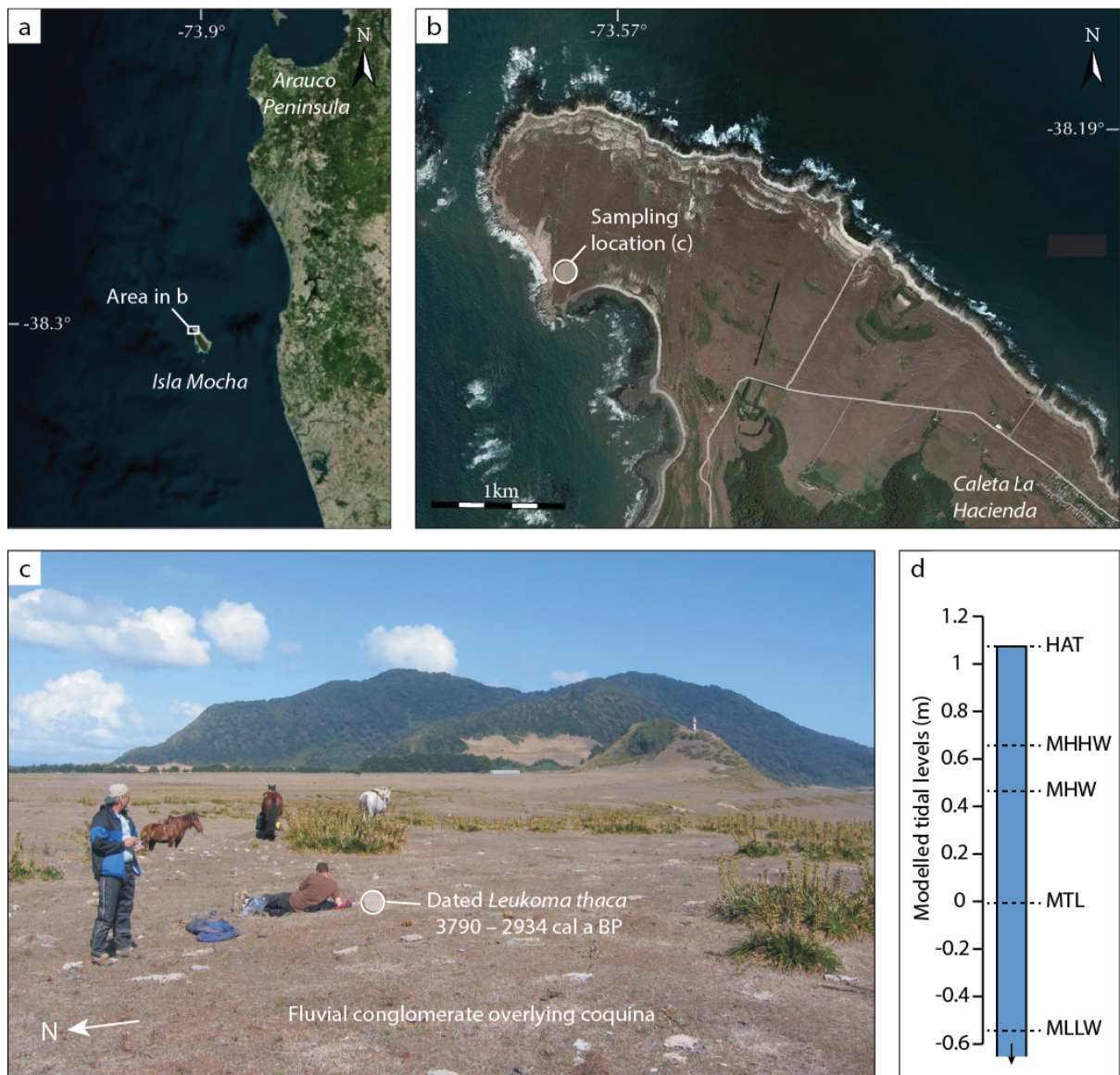
Figure 4: Derivation of the new marine limiting point from Punta Pájaros Niños. a) Location of Isla Mocha and b) the sampling location close to the northern tip of the island. c) Photograph of the sampling site, d) graphical representation of the marine limiting point's indicative meaning (open-ended blue box; below highest astronomical tide) relative to tidal levels at the site modelled using the TPXO8-ATLAS tidal model (Egbert and Erofeeva, 2010). Basemaps in a) and b) are from Bing Maps.

4.4 Pilolcura, Valdivia region

447

448   At Pilolcura (39.6723°S 73.3519°W), a ~1.8 m high section at the landward edge of the contemporary

449   beach exposes a mid to dark grey silt-rich sand underlying ~1.2 m of colluvium (Fig. 5). The silt-rich

450   sand contains a diatom assemblage dominated by freshwater or salt tolerant taxa (*Karayevia*

451   *oblongella* and *Humidophila contenta*). The presence of infrequent brackish (e.g. *Luticola mutica*)

452   and occasional marine species (e.g. *Petroneis marina*) suggests an environment with some tidal

453   influence. The combination of a mixed-salinity diatom assemblage and fine-grained clastic sediments

454   may indicate a tidally influenced lagoon behind a barrier or spit. Comparison of the fossil diatom

455   assemblages with the contemporary distribution of intertidal diatoms in >250 samples from south-

456   central Chile (Hocking et al., 2017) indicates a depositional elevation between MHHW and HAT

457   (Supplementary Information S2). Nevertheless, the modern diatom database does not provide a

458   close analogue for the Pilolcura assemblage, and we consequently assign a more conservative

459   indicative range of between MTL and HAT (Fig. 5e). A fragment of charcoal at a depth of 1.50 m

460   provides a calibrated radiocarbon age of 1089 – 932 cal a BP (Table 2). Taking the reference water

461   level (midpoint between MTL and HAT: 0.55 m) away from the sample elevation (2.47 m), we infer

462   sea level was at 1.92 m. The vertical uncertainty for this index point (0.57 m) is the sum of the

463   uncertainties related to the absolute elevation, the depth within the exposure, and the indicative

464   meaning.

465
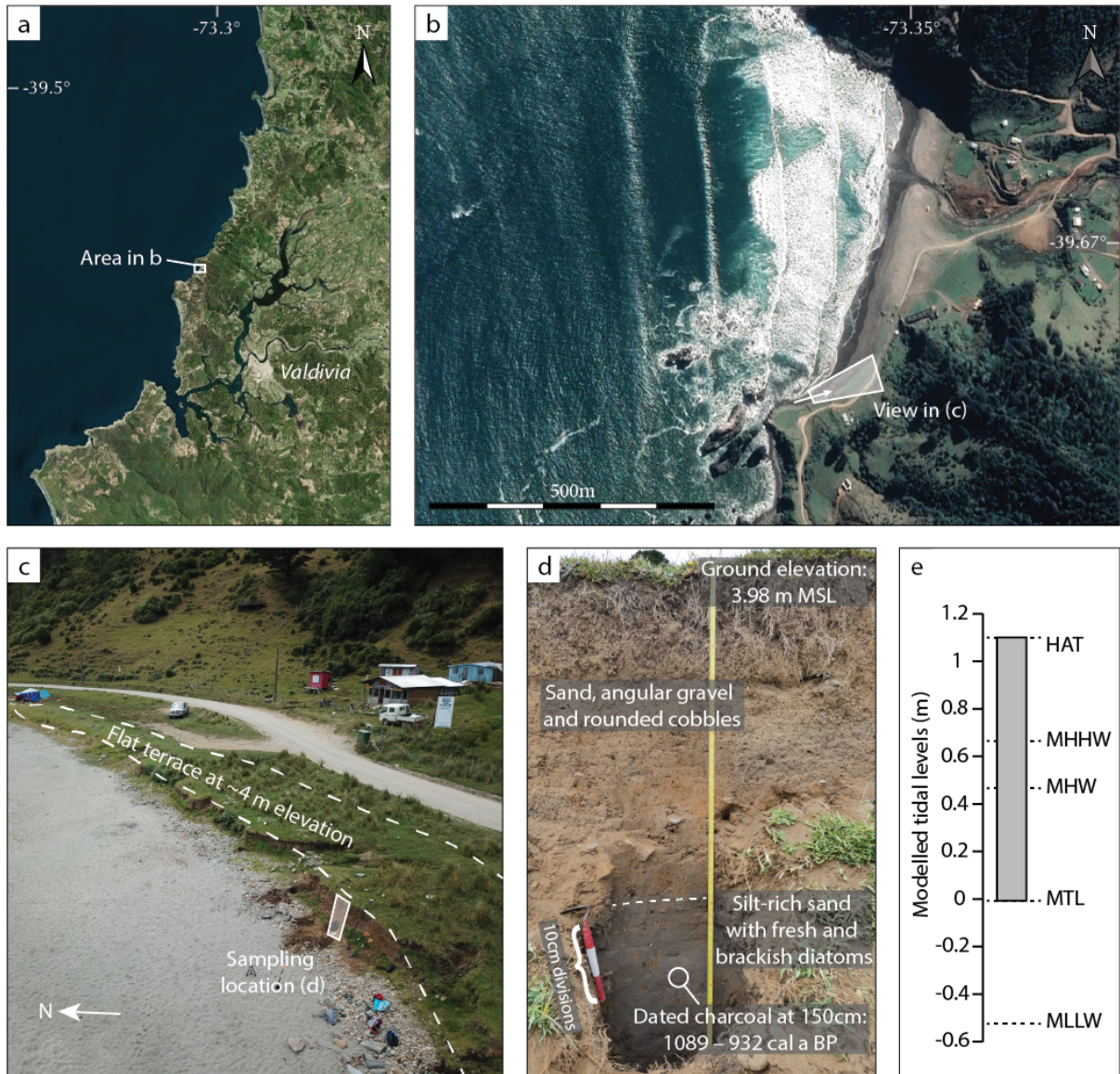
Figure 5: Derivation of the new sea-level index point from Pilolcura. a) – c) Location of the sampling site, d) photograph of the dated section, e) graphical representation of the index point's indicative meaning (grey box; between mean tide level and highest astronomical tide) relative to tidal levels at the site modelled using the TPXO8-ATLAS tidal model (Egbert and Erofeeva, 2010). Basemaps in a) and b) are from Bing Maps.

## 5. The database and regional sea-level histories

475   The Chilean Holocene RSL database (accessible via the data repository) consists of 166 accepted

476   points, of which 79 are index points, 56 are terrestrial limiting points, and 31 are marine limiting

477   points (Fig. 6). We reject a further 53 points for a range of reasons including uncertainties over

478   depositional environments, the possibility of reworking by storms, rivers, tsunamis, or human

479   activity, and chronological outliers identified by the original or subsequent authors. Of the accepted

480   points, 45 are from basal settings, including 28 index points, with the remaining 121 intercalated.

481   Almost 40 % of the accepted points have median ages postdating 1 ka BP, while only 10 points (6 %),

482   nine of which are marine limiting, are older than 6.5 ka BP (Fig. 6). In figure 7, we present sea-level

483   histories for the 11 regions shown in figure 1.

484
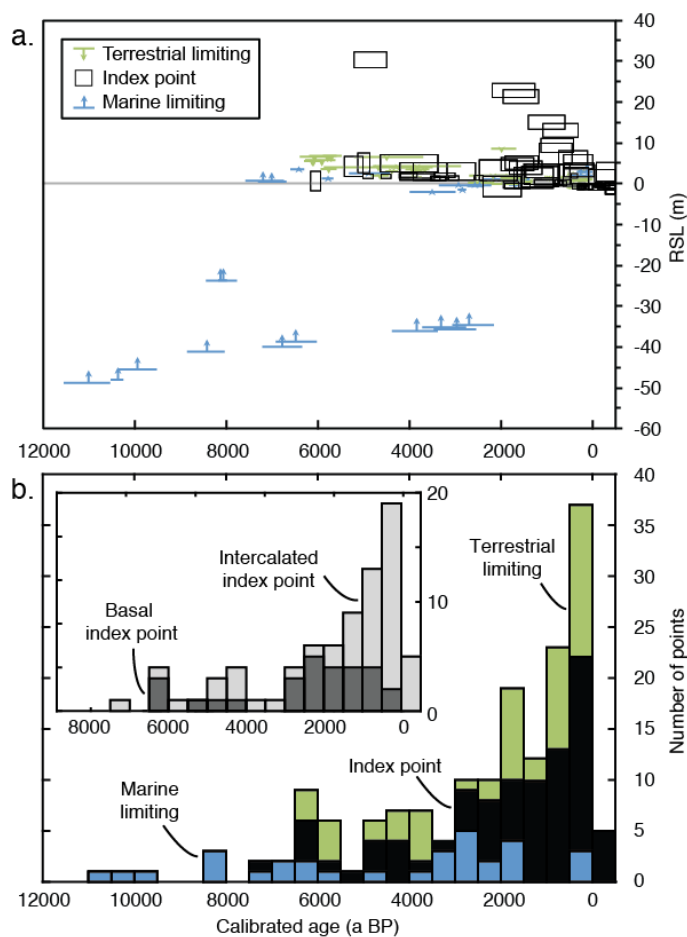
485

486   Figure 6: a. Plot of all accepted sea-level data points in the Chilean database. b. Stacked histogram of

487   the temporal distribution of accepted sea-level data points. Inset compares the distribution of basal

488   and intercalated sea-level index points.

25

489

5.1 Antofagasta (Fig. 7, region 1)

491

The coastline bordering the arid Atacama Desert, covering more than 10 degrees of latitude, currently provides a single Holocene marine limiting point. Leonard and Wehmiller (1991) report three uplifted marine terraces at Caleta Michilla, with only the lowermost having formed during the Holocene. Marine bivalves from this terrace, lying at an elevation of approximately 5.5 m above mean sea level, provide a median age of ~7.2 ka BP. While the authors describe the dated sediments as marine, it is unclear whether the terrace is a raised beach deposited at or above HAT, or a marine deposit with a lower indicative range. Consequently, we consider this sample as a marine limiting point with a reference water level of HAT + 3 m. Our interpretation places RSL above ~0.5 m at this time.

501

5.2 Coquimbo and Tongoy (Fig. 7, region 2)

503

The RSL record of this semi-arid region consists of 11 index points and one marine limiting point from five sites. In contrast to the paucity in other regions, 9 of the 11 index points are from basal settings. The earliest sea-level data point, a ~7.2 ka BP marine limiting point from Estero Tongoy (Ota and Paskoff, 1993), places sea level above ~0.7 m. Index points from prograding sequences of beach ridges in the Bay of Coquimbo (Hart et al., 2017) and beach deposits at El Rincón and Punta Lengua de Vaca, both fringing Tongoy Bay (Ota and Paskoff, 1993), indicate falling sea level after ~5 ka BP from a maximum of at least 5.00 ± 2.09 m. Three index points from Puerto Aldea and El Rincón (Ota and Paskoff, 1993) indicate RSL was between 0 m and 5 m by 2 ka BP, with the large vertical uncertainty associated with the broad indicative range associated with index points from undifferentiated beach environments. Within the last 100 years, two index points from Quebrada de Teatinos, Bay of Coquimbo, place RSL around -1.8 m, with a vertical uncertainty of ~0.7 m (May et

515   al., 2013). We do not incorporate further dated samples from Quebrada Los Chines (Ota and Paskoff,

516   1993), Quebrada de Teatinos, and Quebrada Pachingo (May et al., 2013) due to the potential for

517   reworking or chronological uncertainties identified by the original authors.

518
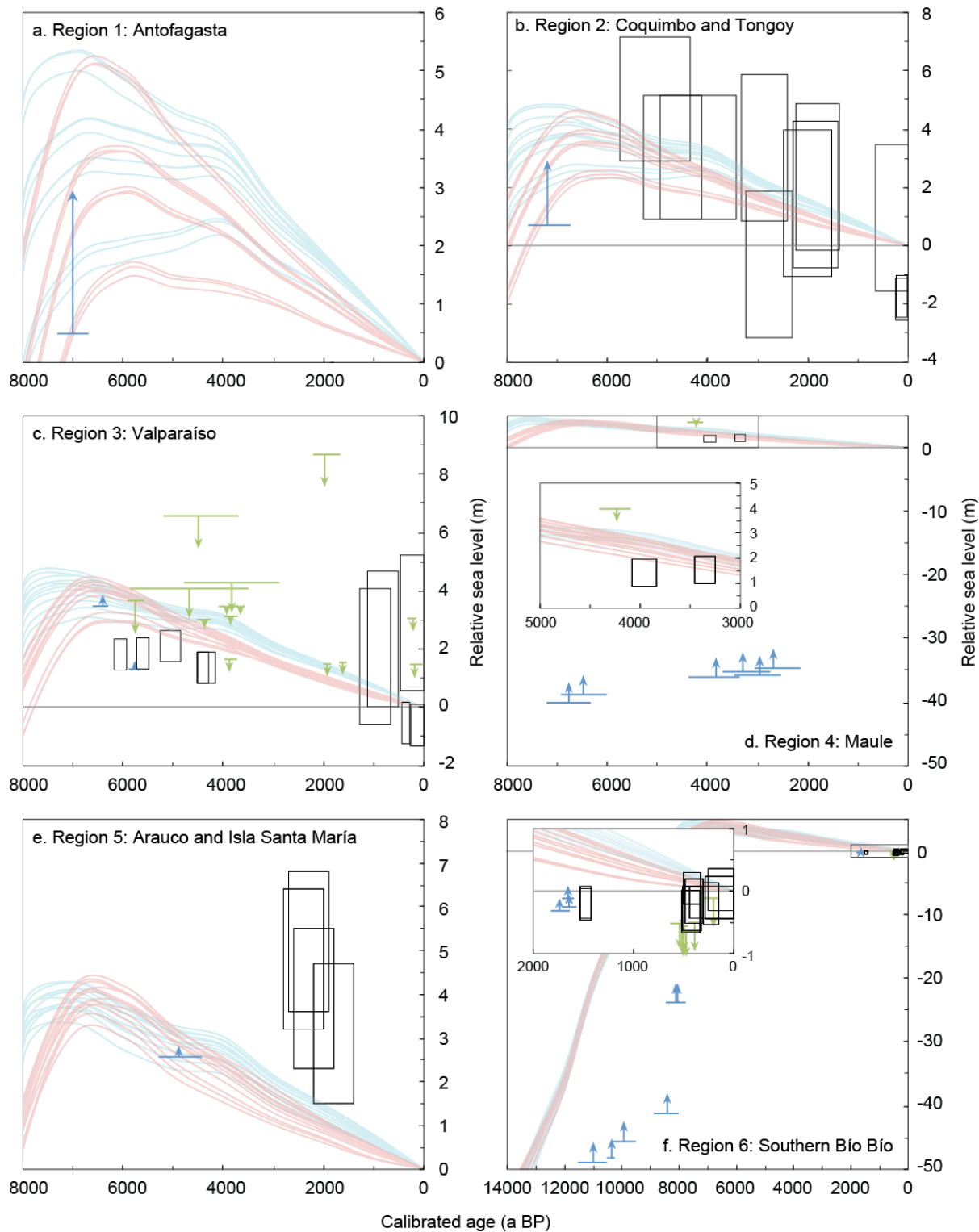
519

520   Figure 7: Regional plots comparing the age – elevation distribution of the sea-level data points with

521   glacial isostatic adjustment model predictions (following Peltier, 2004; Peltier et al., 2015). Sea-level

522   index points are black rectangles, terrestrial and marine limiting points are green T-shaped symbols

523   and blue ⊥-shaped symbols respectively. ICE_5G predictions are light blue curves, ICE_6G

524   predictions are pink curves; for both ice models, we vary the lithospheric thickness between 71 and

525   120 km and the upper mantle viscosity between 5 x 10^{19} Pa s and 2 x 10^{20} Pa s (see section 3.7). Note

526   different x-axis scaling for panel f and variable y-axis scaling between all panels.
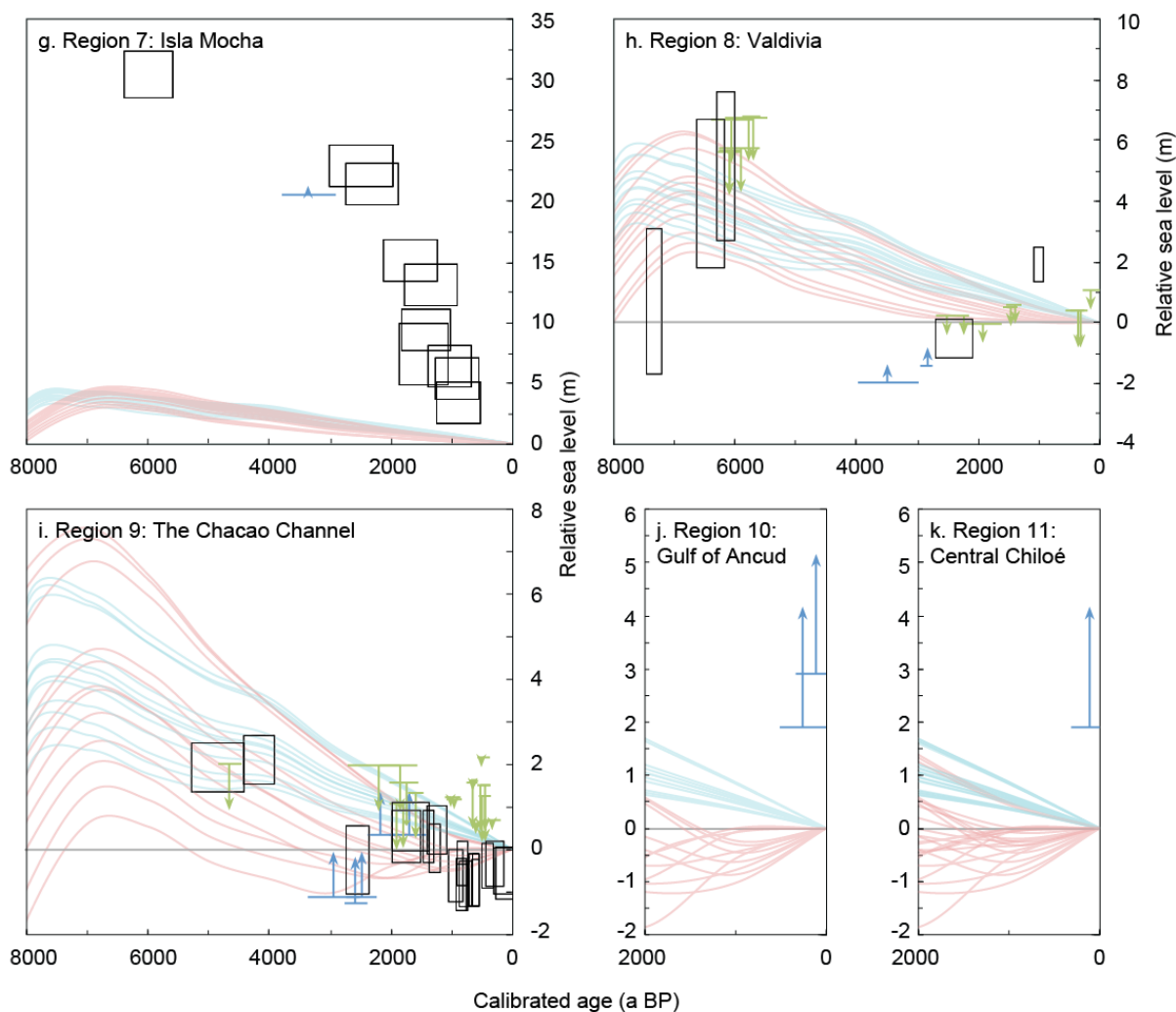
527

528   Figure 7 (continued)

529

530   5.3 Valparaíso (Fig. 7, region 3)

531

28

532 Five sites in the Valparaíso region provide 11 index points, 2 marine limiting and 14 terrestrial

533 limiting points. The earliest evidence comes from Algarrobo, where Encinas et al. (2006) report a

534 silty sandstone containing well-preserved foraminifera, bivalves and gastropods, indicative of a

535 shallow marine environment. This marine limiting point places RSL above ~3.5 m at ~6.4 ka BP. Tidal

536 and freshwater marsh deposits at Quintero, originally investigated for their palaeotsunami record

537 (Dura et al., 2015), provide mid Holocene index points and late Holocene terrestrial limiting points.

538 These data indicate sea level was ~2 m at ~6 ka BP, below 1.65 m at ~3.9 ka BP, and below ~1.5 m

539 during the last 2 ka. Terrestrial limiting points from alluvial deposits underlying the Longotoma dune

540 field concur, indicating sea level below ~3.5 m at ~4 ka BP (May et al., 2015). Within the last

541 millennium, index points from Los Vilos (May et al., 2013) indicate RSL above present, though with

542 large vertical uncertainties, while index points from Pichicuy Bay (May et al., 2013) indicate RSL

543 between -1.3 and 0.2 m.

544

545 5.4 Maule (Fig. 7, region 4)

546

547 In addition to the new terrestrial limiting point from Pelluhue (section 4.1), the sea-level history of

548 this region is further constrained by two index and six marine limiting points from two sites.

549 Frugone-Álvarez et al. (2017) report 11 radiocarbon dates from cores taken from Lago Vichuquén.

550 The lowermost six samples are from sediments interpreted by Frugone-Álvarez et al. (2017) as

551 indicative of marine environments; consequently, the dates constrain the ages of marine limiting

552 points. As the location and elevation of the sill between the lake basin and the sea at the time of

553 deposition is uncertain (today it lies at 2.4 m above EGM2008), we conservatively assume that there

554 was no sill. The accepted marine limiting points place RSL above -40 m at ~6.8 ka BP and above -

555 35 m at ~2.7 ka BP. While the overlying sediments are interpreted as brackish and freshwater

556 (Frugone-Álvarez et al., 2017), radiocarbon dates from these layers cannot be used to constrain sea

557 level due to uncertainties over the isolation of the lake and the role of sediment supply and local

558   tectonics in building the sill. The terrestrial limiting point from Pelluhue places RSL below ~4 m at

559   ~4.2 ka BP, while two index points from El Yolki indicate RSL between 0.85 and 2.1 m between 4 and

560   3 ka BP (Hilleman, 2015; Melnick et al., 2019). We do not consider 13 other radiocarbon dates of

561   ~4 ka BP from Melnick et al. (2019) due to their close proximity to the El Yolki Fault.

562

563   5.5 The Arauco Peninsula and Isla Santa María (Fig. 7, region 5)

564

565   The RSL record consists of four basal index points from Isla Santa María and the new marine limiting

566   point from Tubul. The eastern side of Isla Santa María features a sequence of 21 emerged Holocene

567   beach ridges at elevations between 0.5 m and 8 m. Optically stimulated luminescence ages constrain

568   the timing of the deposition of four of the ridges to the late Holocene, with the oldest dating to 2.1 –

569   2.5 ka BP (Bookhagen et al., 2006). We use the elevation of these four ridges at the locations at

570   which they were sampled for dating to define four index points, noting that the ridges are

571   progressively tilted to the northwest at a rate estimated by Bookhagen et al. (2006) of

572   0.022 ± 0.002 °/ka. These index points place RSL between 3.11 m and 5.21 m, with vertical

573   uncertainties of ± 1.6 m. As described in section 4.2, a marine limiting point from Tubul places sea

574   level above 2.57 m at ~5 ka BP.

575

576   Although two shells have been dated on the coastal plains at Coronel and Carampangue (Isla et al.,

577   2012), we are unable to derive index or limiting points. Because both dates relate to broken shells of

578   unknown species, we cannot establish whether these shells are originally from subtidal, intertidal or

579   supratidal environments and whether they are in-situ or have been subsequently transported.

580

581   5.6 Southern Bío Bío (Fig. 7, region 6)

582

583   The RSL history of the Southern Bío Bío region is constrained by 10 index, 8 terrestrial limiting, and 9

584   marine limiting points. We derive two marine limiting points from Lake Lanalhue and four marine

585   limiting points from Lake Lleu Lleu (Stefer et al., 2010). The dated samples, ranging from 8 to 11 ka

586   BP, come from clastic sediments containing marine shells and foraminifera at elevations of between

587   -22 m and -47 m. While the basins also contain subsequent lacustrine sedimentary infills, we cannot

588   derive terrestrial limiting points from 17 further radiocarbon dates from these intervals due to the

589   uncertain rate of tectonic uplift and coeval erosion of the sill that separates the contemporary lake

590   from the Pacific. Organic silt and peat layers at Quidico (38.2°S) and Tirúa (38.3°S) provide 21 further

591   sea-level data points, including 10 index points (Ely et al., 2014; Dura et al., 2017; Hong et al., 2017).

592   The accepted ages are all within the last 1.9 ka and lie between -0.6 m and 0.4 m.

593

594   5.7 Isla Mocha (Fig. 7, region 7)

595

596   Ten index points, all of them from basal settings, and one marine limiting point constrain the sea-

597   level history of Isla Mocha. The island, lying approximately 30 km off the coast of mainland Chile,

598   features a kilometre-wide fringe of uplifted Holocene beach ridges (Nelson and Manley, 1992). Two

599   studies provide radiocarbon ages from either shell fragments or intact shells from beach ridges at

600   elevations up to 33 m (Kaizuka et al., 1973; Nelson and Manley, 1992). Following Nelson and Manley

601   (1992), we exclude several of these ages due to the probability of reworking of older shell material.

602   The 10 accepted index points, along with our new marine limiting point from the north of the island

603   at Punta Pájaros Niños, place RSL around 30 m at ~6 ka BP, falling to ~23 m at ~2.5 ka BP and

604   subsequently falling at a faster rate to below 5 m at ~0.9 ka BP.

605

606   5.8 Valdivia (Fig. 7, region 8)

607

608   Five index, two marine limiting and 14 terrestrial limiting points provide the RSL record for the

609   Valdivia region. The oldest index point, coming from shell-bearing sands indicative of a beach

610   environment at Isla Mancera (Villalobos Silva, 2005), dates to ~7.3 ka BP and places RSL between -

611   1.7 m and 3.1 m, with the large vertical uncertainty reflecting a broad indicative range. Index points

612   from beach sediments and terrestrial limiting points from aeolian dunes at Chan Chan indicate RSL

613   was between 1.8 m and 7.6 m at ~6 ka BP (Pino and Navarro, 2005). Between ~3.5 ka BP and

614   present, index and marine limiting points from tidally influenced clastic sediments and terrestrial

615   limiting points from freshwater soils in the Las Coloradas inlet and Isla Mancera place RSL between -

616   2 m and 1 m (Villalobos Silva, 2005; Nelson et al., 2009). The new index point from Pilolcura places

617   RSL at 1.92 ± 0.57 m, ~1 ka BP.

618

619   5.9 The Chacao Channel (Fig. 7, region 9)

620

621   The coast of northern Chiloé and the adjacent continental coast around the Río Maullín, collectively

622   termed the Chacao Channel region, provide 26 index, five marine limiting and 19 terrestrial limiting

623   points. These points stem from palaeoseismic studies of coastal lowlands and marshes (Atwater et

624   al., 1992; Cisternas et al., 2005; 2017; Garrett et al., 2015). The earliest sea-level data come from

625   Chocoi, where tidal marsh peat layers exposed in a sea cliff attest to RSL ~2 m above present

626   between 5 and 4 ka BP (Atwater et al., 1992). A subsequent fall in RSL is recorded by tidal marsh

627   deposits at Maullín (Cisternas et al., 2005), Dadi, and Puente Cariquilda (Atwater et al., 1992). Six

628   index points from these locations place RSL between -1 m and 1 m during the period between 3 and

629   1 ka BP. Terrestrial limiting points in this interval place sea level below 2 m, with marine limiting

630   points indicating sea level above -1.5 m at ~3 ka BP and above 0.35 m at ~2 ka BP. Twelve index

631   points from Chucalen (Garrett et al., 2015) and six from Maullín (Cisternas et al., 2005) indicate RSL

632   was ~1 m below present at ~0.9 ka BP, with the subsequent rise to present overprinted by metre-

633   scale coseismic subsidence events resulting from great subduction earthquakes (Garrett et al.,

634   2015). Terrestrial limiting points for the last 1 ka from Maullín (Cisternas et al., 2005) and Cocotué

635   (Cisternas et al., 2017) indicate sea level below elevations varying between 2.3 m and 0.7 m.

636

637   5.10 Reloncaví Sound and Gulf of Ancud (Fig. 7, region 10)

638

639   Two marine limiting points constrain the RSL history of the semi-enclosed coastlines to the northeast

640   of Chiloé. Both points come from Bahía Hualaihué, where intertidal or subtidal bivalves in living

641   position indicate sea levels above 1.90 m and 2.90 m (Hervé and Ota, 1993). Both samples have

642   median ages within the last 0.3 ka. We reject further dated shells from Bahía Hualaihué and sites at

643   Ralún at the head of Fiordo Reloncaví and the Cholgo Canal (Hervé and Ota, 1993) due to the

644   possibility of reworking by extreme waves or human activity.

645

646   5.11 Central Chiloé (Fig. 7, region 11)

647

648   Central Chiloé provides a single marine limiting point, with no further accepted sea-level data from

649   southern Chiloé, Isla Guafo or the continental coastline or islands of the Gulf of Corcovado. At Cucao,

650   on the western coast of Chiloé, Hervé and Ota (1993) report subtidal bivalves in living position

651   indicating RSL above 1.89 m. Recalibration of the radiocarbon age provides a range of 325 cal a BP to

652   present. We reject one dated shell from Nercón on the eastern coast of Chiloé (Hervé and Ota, 1993)

653   due to the possibility of reworking.

654

655   **6. Discussion**

656

657   6.1 Glacial isostatic adjustment

658

33

659   The Chilean sea-level database includes 166 accepted sea-level data points. Nevertheless, as these

660   are unevenly spread across 2200 km of coast (20 degrees of latitude), our current knowledge of past

661   sea levels is spatially variable and, in some areas (regions 1, 4, 10, 11, and all remaining stretches of

662   coastline that lack any data), highly limited. Nonetheless, the presence of several data-rich regions

663   with well-constrained sea-level histories highlights a high degree of spatial variability in Holocene

664   RSL change and provides an opportunity to make a preliminary investigation into the processes

665   driving these changes. To this end, we compare the distribution of sea-level data with RSL

666   predictions from a suite of GIA models (Fig. 7).

667

668   GIA model predictions display a high degree of variability along the Chilean coastline. The two

669   northernmost regions are characterised by modelled mid Holocene highstands 1.5 − 5.5 m above

670   present between 7 ka and 4 ka (Fig. 7a-b). The five central regions between Valparaíso and Isla

671   Mocha share modelled highstands 3 − 6 m above present at 7 ka or 6 ka (Figs. 7c-g). The predictions

672   for the four southernmost regions, around Valdivia and Isla de Chiloé, display maxima at elevations

673   between 0.5 and 8 m above present at 8 ka or 7 ka, with a high degree of variability between

674   different models (Figs. 7h-k). Unlike in regions 1 − 8, where all models predict RSL fall following the

675   highstand, models that adopt low values for upper mantle viscosity, when combined with the ICE-6G

676   ice model, predict RSL rise over the last 1 − 3 ka in regions 9 − 11 (Figs. 7i-k).

677

678   For the majority of Chilean regions, the database of sea-level data points and the GIA model

679   predictions provide a coherent account of the pattern of Holocene RSL change. No additional factors

680   are required to explain the age and elevation of data points in regions 1 and 4 (Fig. 7); however, this

681   may reflect the paucity of data in these regions. In regions 2, 3, 6, 8, and 9, decimetre- to metre-

682   scale vertical motions associated with centennial-scale earthquake cycle deformation would be

683   sufficient to account for the small disparities between sea-level data and GIA model predictions. In

684   the remaining regions—Arauco and Isla Santa María (region 5), Isla Mocha (region 7), the Gulf of

685   Ancud (region 10), and Central Chiloé (region 11)—index and marine limiting points consistently lie

686   above the GIA predictions, suggesting the importance of other factors at these locations. In the

687   following section, we explore the potential for millennial-scale secular tectonic uplift to account for

688   these differences.

689

690   6.2 Regional tectonic uplift

691

692   Allowing for centennial-scale earthquake deformation cycles, we apply linear corrections to the RSL

693   data to improve the fit with the GIA model predictions (see section 3.7 and Supplementary

694   information S3). We summarise the range of acceptable linear corrections for each region in Figure 8

695   and compare these with independently derived estimates of multi-millennial-scale tectonic uplift.

696   We note that our linear corrections provide a first approximation of tectonic uplift rates, but also

697   reflect the cumulative effects of other processes including sediment compaction and sediment

698   isostasy, among other local processes. We make an initial exploration of the possible role of tectonic

699   uplift and other processes in each region in the following paragraphs.

700

701   As previously stated, once centennial-scale deformation cycles are accounted for, no additional

702   correction is required to explain data-model discrepancies in regions 1, 2, 3, 4, 6, 8, and 9. However,

703   a range of positive and/or negative corrections may still provide acceptable fits with the model

704   predictions. In regions 1 and 2, our accepted ranges of linear corrections (>-0.8 m ka^{-1} and -0.3 –

705   0.6 m ka^{-1} respectively) overlap with Melnick's (2016) independent estimates based on a landscape

706   evolution model for the central Andean rasa (Fig. 8). In region 3, as mid-Holocene index points lie

707   below GIA model predictions, we invoke negative rates of -0.3 to 0 m ka^{-1} (subsidence) (Fig. 8). The

708   slight discrepancy between this and Melnick's (2016) tectonic uplift rate of 0.06 ± 0.02 m ka^{-1} could

709   indicate sediment compaction affects the intercalated index points from the organic-rich lowland at

710   Quintero (Dura et al., 2015).

       35

711
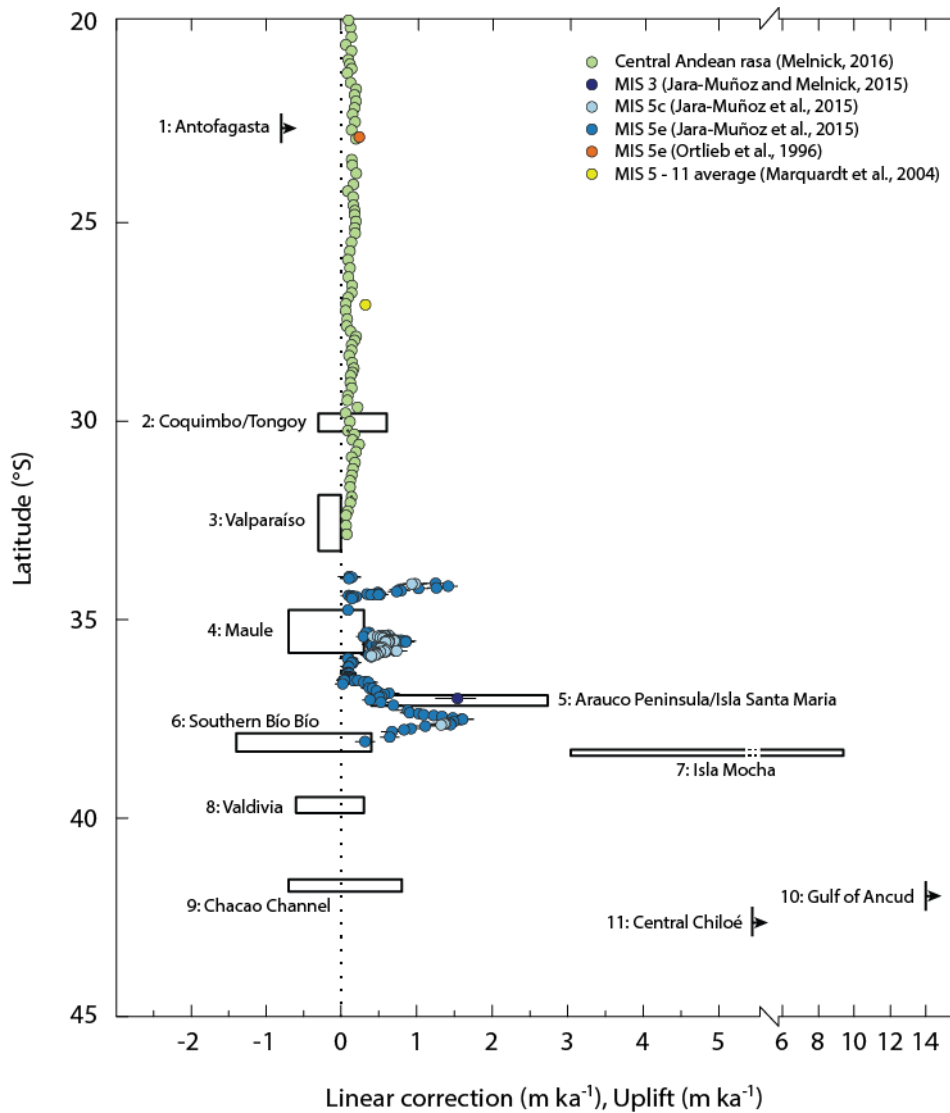
712

713   Figure 8: Comparison of best-fit linear correction rates (black rectangles) required to remove the

714   misfit between sea-level data and a suite of glacial isostatic adjustment models with independently

715   derived estimates of tectonic uplift (coloured circles). Sea-level data and GIA models for the 11

716   regions are shown in Figure 7 and the linear corrections are illustrated in Supplementary Information

717   S3.

718

719   Accepted linear correction rates for region 4 range from -0.7 m ka^{-1} (subsidence) to 0.3 m ka^{-1} (uplift)

720   (Fig. 8). Jara-Muñoz et al. (2015) suggest higher tectonic uplift rates in the region since the last

721   interglacial, with rates of 0.4 to 0.8 m ka^{-1} associated with a long-wavelength upwarping zone and

722   the activity of three major crustal normal faults that intersect the coastline and displace the marine

723   isotope stage (MIS) 5 marine terraces. Correcting the sea-level data for such high tectonic uplift rates

724   would lower index points below our model predictions. This could 1) potentially indicate a greater

725   level of spatial variability in uplift rates associated with local crustal structures than previously

726   identified, 2) suggest that late Holocene tectonic uplift rates have not been sustained over longer

727   timescales, or 3) reflect spatial complexity in Earth rheology that is not accounted for by GIA models.

728   Uplift rates inferred from last interglacial terraces do not account for local departures from the

729   global eustatic sea level associated with GIA (Creveling et al., 2015), potentially also contributing to

730   the disparity with the inferred Holocene rates.

731

732   A linear correction of between 0.4 and 2.7 m ka^{-1} (uplift) could account for the elevated position of

733   the four index points from Isla Santa María with respect to the GIA model predictions for region 5

734   (Figs. 7e, 8). Jara-Muñoz and Melnick (2015) concur, inferring a tectonic uplift rate of 1.5 ± 0.3 m ka^{-1}

735   from MIS 3 sediments on Isla Santa María. We note that continued debate over MIS 3 sea levels may

736   lead to a reassessment of this rate (Pico et al., 2017; Dalton et al., 2019). Jara-Muñoz et al. (2015)

737   indicate lower post-MIS 5e tectonic uplift rates for the Arauco Peninsula, including ~0.3 m ka^{-1} at the

738   latitude of our site at Tubul. Neither the MIS 5e nor the MIS 3 uplift rates account for local GIA-

739   induced departures from global eustasy (Creveling et al., 2015).

740

741   Linear corrections of -1.4 m ka^{-1} (subsidence) to 0.4 m ka^{-1} (uplift) provide the best fit for the late

742   Holocene in region 6 (Fig. 8). Based on comparison of the early Holocene record from lakes Lanalhue

743   and Lleu Lleu with "global" sea-level curves, Stefer et al. (2010) inferred tectonic uplift rates in the

744   region of 0.5 m ka^{-1}. We update this analysis by comparing reassessed sea-level data from the two

745   lakes with the suite of GIA model predictions for this particular location. As a result of isostatic

746   rebound, the model predictions for this region lie substantially above farfield RSL curves, implying

747   that the uplift rates derived in the original study were overestimated. While the Lanalhue and Lleu

37

748 Lleu marine limiting points lie above the global curves (Stefer et al., 2010), they lie below the local

749 model predictions (Fig. 7f and supplementary figure S3f). Consequently, no tectonic uplift is required

750 to reconcile the observations of Stefer et al. (2010) with the model predictions, in contrast to the

751 conclusions of the original study.

752

753 Sea-level index points from Isla Mocha lie above the suite of GIA model predictions for region 7 (Fig.

754 7g). Linear corrections of between 3 m ka^{-1} and 9.5 m ka^{-1} reduce the misfit, with the highest uplift

755 rates required to reconcile data from the last 3000 years (Fig. 8). No single rate can bring every index

756 point within the suite of model predictions, potentially indicating an increase in uplift rates during

757 the Holocene, as identified by Nelson and Manley (1992). The rapid localised tectonic uplift of Isla

758 Mocha, contrasting with the adjacent southern Bío Bío region, may reflect aseismic and/or seismic

759 slip on imbricate thrust faults within the South American Plate (von Heune et al., 1985; Nelson and

760 Manley, 1992).

761

762 Linear corrections of -0.6 m ka^{-1} (subsidence) to 0.3 m ka^{-1} (uplift) provide an acceptable fit between

763 data and models in region 8, with a similar range of -0.7 m ka^{-1} (subsidence) to 0.8 m ka^{-1} (uplift) for

764 region 9 (Fig. 8). Notably, in region 9, index points for the last 1000 years are below present sea

765 level. This pattern, apparent from two sites separated by ~40 km, was previously recognised by

766 Garrett et al. (2015) and tentatively attributed to incomplete interseismic uplift following coseismic

767 subsidence during the 1960 earthquake. Interseismic uplift rates have been slowly increasing over

768 the past few decades (Melnick et al. 2018), a trend that would raise the dated sediments back

769 towards present sea level. In addition, effects at a local scale such as sediment compaction, or at a

770 larger scale such as neoglacial forebulge collapse, might influence RSL in this region over the last

771 millennium. While GIA model predictions generated using the ICE-6G ice model (Peltier et al., 2015)

772 in combination with relatively weak upper mantle viscosities replicate a late Holocene sea-level rise,

773 this signal may occur due to the low spatial resolution of the model and its inability to fully resolve

774   water loading and shoreline changes in this landscape of deep marine gulfs and mountains. The

775   cause of late Holocene sea-level rise in this region remains uncertain; nevertheless, its occurrence

776   provides accommodation space and may explain the preservation of palaeoseismic evidence at sites

777   in the region (Cisternas et al., 2005; 2017; Garrett et al., 2015).

778

779   Hervé and Ota (1993) inferred extremely fast tectonic uplift rates of 5 to 10 m ka^{-1} in regions 10 and

780   11 during the late Holocene. While we have rejected four of the seven dates in these regions due to

781   the possibility for reworking by extreme waves or human activity, the remaining three marine

782   limiting points require linear correction rates of > 14 m ka^{-1} (region 10) and > 5.5 m ka^{-1} (region 11)

783   to bring them in line with the model predictions (Fig. 8). While rapid uplift in region 10 may be

784   associated with the Liquiñe-Ofqui fault zone, further data are required to corroborate and extend

785   the record of RSL change in the continental region east of Isla de Chiloé.

786

787   6.3 Data paucity and areas for future focus

788

789   The Chilean sea-level database highlights the scarcity of sea-level data from northern Chile. Few

790   studies have focussed on the relative sea-level history in this region, or on allied endeavours that

791   may produce sea-level data points, such as coastal palaeoseismology. We attribute this lack to the

792   rarity of coastal fine-grained sedimentary depocentres and the terrestrial organic fossils to date

793   resulting from the region's aridity. To overcome this problem, future studies may consider rocky-

794   shore geomorphic markers and beach or beach ridge deposits that can be dated using marine shells

795   or through luminescence approaches. Such features have successfully provided sea-level data in

796   central Chile (Nelson and Manley, 1992; Bookhagen et al., 2006; Hart et al., 2017) and are present

797   along the coast of northern Chile. Future work should also focus on providing appropriate local

798   estimates of the indicative meaning of such features through surveying analogous modern sea-level

799   indicators and relating these to tidal datums.

39

800

801   While central and south-central Chile are more comprehensively represented in the database, the

802   majority of sea-level data points are limited to the late Holocene and, particularly, the last 2 ka (Fig.

803   6). Consequently, there are few data to constrain key features of RSL history of this region. The

804   height and timing of the mid-Holocene highstand remains a major uncertainty, with proxy

805   reconstructions and GIA modelling indicating elevations between 2 and 6 m at Valdivia and between

806   0.5 and 7.5 m in the vicinity of the Chacao Channel.

807

808   7. Conclusions

809

810   The Chilean Holocene sea-level database presented in this paper provides a systematic, quality

811   controlled, and internationally comparable database of sea-level data from the tectonically active

812   coast of north, central and south-central Chile (18.5 – 43.6°S). We reinterpret indicative meanings

813   (the relationship between a sea-level indicator and contemporaneous tidal levels), recalibrate ages,

814   and fully assess all sources of error for sea-level indicators stemming from research into relative sea-

815   level change, coastal palaeoseismology, palaeoclimatology, and archaeology. Much of the

816   information on past sea levels provided by these sources has previously been overlooked. Our

817   database summarises 166 accepted points, including 79 index points, 31 marine limiting points, and

818   56 terrestrial limiting points. We reject a further 53 data points due to ambiguities over the

819   interpretation of depositional environments, the possibility of reworking by storm, fluvial, tsunami,

820   or human activity, along with chronological inconsistencies.

821

822   The database includes sea-level data from four new sites presented here for the first time: Pelluhue

823   (south of Constitución), Tubul (northern Arauco Peninsula), Punta Pájaros Niños (northern Isla

824   Mocha), and Pilolcura (north of Valdivia). These sites illustrate how a range of different data sources,

825   including alluvial deposits, marine shells, and intertidal sediments can provide constraints on past

826   sea level. Collectively, the new sites provide two marine limiting points, one terrestrial limiting point

827   and one index point.

828

829   Combining new and reassessed data, we use the database to describe relative sea-level histories for

830   11 coastal regions of Chile, noting the spatial inhomogeneity of the data. These histories highlight

831   substantial spatial differences in Holocene relative sea level: while the mid Holocene was

832   characterised by sea level above present in all regions, elevations vary from <5 m to 30 m.

833   Comparison of sea-level data with a suite of glacial isostatic adjustment models enables us to assess

834   the processes driving RSL change and highlights regions where millennial-scale tectonic deformation

835   may cause the data to significantly diverge from model predictions (particularly Isla Santa María, Isla

836   Mocha, and regions close to the Liquiñe-Ofqui fault zone). Uplift rates likely exceed 1 m ka^{-1} in these

837   regions and may be an order of magnitude greater over centennial timescales. We identify that no

838   net uplift is required to reconcile data and model predictions in many areas, including the southern

839   Bío Bío region, in contrast to the findings of an earlier study (Stefer et al., 2010).

840

841   We highlight northern Chile and the early to mid Holocene in all regions as particularly data poor.

842   Future efforts to address these data gaps will continue to assist efforts to address questions over the

843   driving mechanisms of sea-level variability (Khan et al., 2019). Furthermore, with the spatiotemporal

844   distribution of coastal archaeological and palaeoseismic evidence closely related to relative sea-level

845   change (Dickinson, 2011; Dura et al., 2016), the current Chilean sea-level database and future

846   advances in constraining RSL histories along the Chilean coast will support future research in these

847   and other fields.

41

862

863 **Data availability**

864 The Chilean sea-level database is available via Mendeley Data:

865 http://dx.doi.org/10.17632/9459bd6gpt

866

867 **References**

868

869 Aniya, M., 1996. Holocene variations of Ameghino Glacier, southern Patagonia. The Holocene 6,

870   247–252.

871 Araneda, A., Torrejón, F., Aguayo, M., Torres, L., Cruces, F., Cisternas, M., Urrutia, R., 2007. Historical

872   records of San Rafael glacier advances (North Patagonian Icefield): another clue to 'Little Ice Age'

873   timing in southern Chile? The Holocene 17, 987–998.

42

874   Atwater, B.F., Núñez, H.J., Vita-Finzi, C., 1992. Net late Holocene emergence despite earthquake-

875   induced submergence, south-central Chile. Quaternary International 15, 77–85.

876   Barrientos, S., 2007. Earthquakes in Chile. The geology of Chile. The Geological Society, London 263–

877   287.

878   Bentley, M.J., McCulloch, R.D., 2005. Impact of neotectonics on the record of glacier and sea level

879   fluctuations, Strait of Magellan, southern Chile. Geografiska Annaler: Series A, Physical Geography

880   87, 393–402.

881   Bernard, F.R., 1983. Catalogue of the living bivalvia of the eastern Pacific Ocean: Bering Strait to

882   Cape Horn. Canadian Special Publication of Fisheries and Aquatic Sciences.

883   Bertrand, S., Hughen, K., Lamy, F., Stuut, J.B., Torejon, F., Lange, C., 2012. Precipitation as the main

884   driver of Neoglacial fluctuations of Gualas glacier, Northern Patagonian Icefield. Climate of the Past

885   8, 1–16.

886   Bloom, A.L., 1977. Atlas of Sea-level Curves: IGCP Project 61. International Geological Correlation

887   Program.

888   Bookhagen, B., Echtler, H.P., Melnick, D., Strecker, M.R., Spencer, J.Q.G., 2006. Using uplifted

889   Holocene beach berms for paleoseismic analysis on the Santa María Island, south-central Chile.

890   Geophysical Research Letters 33.

891   Brain, M.J., Long, A.J., Woodroffe, S.A., Petley, D.N., Milledge, D.G., Parnell, A.C., 2012. Modelling

892   the effects of sediment compaction on salt marsh reconstructions of recent sea-level rise. Earth

893   and Planetary Science Letters 345, 180–193.

894   Bronk Ramsey, C., 2009. Bayesian analysis of radiocarbon dates. Radiocarbon 51, 337–360.

895   Caldenius, C.C.Z., 1932. Las Glaciaciones Cuaternarias en la Patagonia y Tierra del Fuego: Una

896   investigación regional, estratigráfica y geocronológica.—Una comparación con la escala

897   geocronológica sueca. Geografiska Annaler 14, 1–164.

898   Cembrano, J., Hervé, F., Lavenu, A., 1996. The Liquiñe Ofqui fault zone: a long-lived intra-arc fault

899   system in southern Chile. Tectonophysics 259, 55–66.

43

900 Cisternas, M., Garrett, E., Wesson, R.L., Dura, T., Ely, L.L., 2017. Unusual geologic evidence of coeval

901   seismic shaking and tsunamis shows variability in earthquake size and recurrence in the area of the

902   giant 1960 Chile earthquake. Marine Geology 385, 101–113.

903 Cisternas, M., Atwater, B.F., Torrejón, F., Sawai, Y., Machuca, G., Lagos, M., Eipert, A., Youlton, C.,

904   Salgado, I., Kamataki, T., 2005. Predecessors of the giant 1960 Chile earthquake. Nature 437, 404–

905   407.

906 Creveling, J.R., Mitrovica, J.X., Hay, C.C., Austermann, J., Kopp, R.E., 2015. Revisiting tectonic

907   corrections applied to Pleistocene sea-level highstands. Quaternary Science Reviews 111, 72–80.

908 Dalton, A.S., Finkelstein, S.A., Forman, S.L., Barnett, P.J., Pico, T., Mitrovica, J.X., 2019. Was the

909   Laurentide ice sheet significantly reduced during marine isotope stage 3? Geology 47, 111–114.

910 Denton, G.H., Lowell, T. V, Heusser, C.J., Schlüchter, C., Andersen, B.G., Heusser, L.E., Moreno, P.I.,

911   Marchant, D.R., 1999. Geomorphology, stratigraphy, and radiocarbon chronology of Llanquihue

912   Drift in the area of the Southern Lake District, Seno Reloncaví, and Isla Grande de Chiloé, Chile.

913   Geografiska Annaler: Series A, Physical Geography 81, 167–229.

914 Dickinson, W.R., 2011. Geological perspectives on the Monte Verde archeological site in Chile and

915   pre-Clovis coastal migration in the Americas. Quaternary Research 76, 201–210.

916 Dura, T., Cisternas, M., Horton, B.P., Ely, L.L., Nelson, A.R., Wesson, R.L., Pilarczyk, J.E., 2015. Coastal

917   evidence for Holocene subduction-zone earthquakes and tsunamis in central Chile. Quaternary

918   Science Reviews 113, 93–111.

919 Dura, T., Engelhart, S.E., Vacchi, M., Horton, B.P., Kopp, R.E., Peltier, W.R., Bradley, S., 2016. The role

920   of Holocene relative sea-level change in preserving records of subduction zone earthquakes.

921   Current Climate Change Reports 2, 86–100.

922 Dura, T., Horton, B.P., Cisternas, M., Ely, L.L., Hong, I., Nelson, A.R., Wesson, R.L., Pilarczyk, J.E.,

923   Parnell, A.C., Nikitina, D., 2017. Subduction zone slip variability during the last millennium, south-

924   central Chile. Quaternary Science Reviews 175, 112–137.

925   Egbert, G.D., Erofeeva, S.Y., 2010. The OSU TOPEX/Poseidon Global Inverse Solution TPXO. Oregon

926   State University.

927   Ehlers, J., Gibbard, P.L., Hughes, P.D., 2011. Quaternary glaciations-extent and chronology: a closer

928   look. Elsevier.

929   Ely, L.L., Cisternas, M., Wesson, R.L., Dura, T., 2014. Five centuries of tsunamis and land-level

930   changes in the overlapping rupture area of the 1960 and 2010 Chilean earthquakes. Geology 42,

931   995–998. doi:10.1130/G35830.1

932   Encinas, A., Hervé, F., Villa-Martínez, R., Nielsen, S.N., Finger, K.L., Peterson, D.E., 2010. Finding of a

933   Holocene marine layer in Algarrobo (33 22'S), central Chile. Implications for coastal uplift. Andean

934   Geology 33, 339–345.

935   Engelhart, S.E., Vacchi, M., Horton, B.P., Nelson, A.R., Kopp, R.E., 2015. A sea-level database for the

936   Pacific coast of central North America. Quaternary Science Reviews 113, 78–92.

937   Farías, M., Vargas, G., Tassara, A., Carretier, S., Baize, S., Melnick, D., Bataille, K., 2010. Land-level

938   changes produced by the Mw 8.8 2010 Chilean earthquake. Science 329, 916.

939   Farrell, W.E., Clark, J.A., 1976. On Postglacial Sea Level. Geophysical Journal International 46, 647–

940   667.

941   Freed, A.M., Hashima, A., Becker, T.W., Okaya, D.A., Sato, H., Hatanaka, Y., 2017. Resolving depth-

942   dependent subduction zone viscosity and afterslip from postseismic displacements following the

943   2011 Tohoku-oki, Japan earthquake. Earth and Planetary Science Letters 459, 279–290.

944   Frugone-Álvarez, M., Latorre, C., Giralt, S., Polanco-Martínez, J., Bernárdez, P., Oliva-Urcia, B.,

945   Maldonado, A., Carrevedo, M.L., Moreno, A., Delgado Huertas, A., 2017. A 7000-year high-

946   resolution lake sediment record from coastal central Chile (Lago Vichuquén, 34° S): implications for

947   past sea level and environmental variability. Journal of Quaternary Science 32, 830–844.

948   García-Artola, A., Stéphan, P., Cearreta, A., Kopp, R.E., Khan, N.S., Horton, B.P., 2018. Holocene sea-

949   level database from the Atlantic coast of Europe. Quaternary Science Reviews 196, 177–192.

950   García, J.L., 2012. Late Pleistocene ice fluctuations and glacial geomorphology of the Archipiélago de

951   Chiloé, southern Chile. Geografiska Annaler: Series A, Physical Geography 94, 459–479.

952   Garrett, E., Shennan, I., Woodroffe, S.A., Cisternas, M., Hocking, E.P., Gulliver, P., 2015.

953   Reconstructing paleoseismic deformation, 2: 1000 years of great earthquakes at Chucalén, south

954   central Chile. Quaternary Science Reviews 113, 112–122.

955   Garrett, E., Brader, M., Melnick, D., Bedford, J., Aedo, D., 2019. First Field Evidence of Coseismic

956   Land-Level Change Associated with the 25 December 2016 Mw 7.6 Chiloé, Chile, Earthquake.

957   Bulletin of the Seismological Society of America 109, 87–98.

958   Glasser, N.F., Harrison, S., Winchester, V., Aniya, M., 2004. Late Pleistocene and Holocene

959   palaeoclimate and glacier fluctuations in Patagonia. Global and Planetary Change 43, 79–101.

960   Glasser, N.F., Jansson, K.N., Harrison, S., Kleman, J., 2008. The glacial geomorphology and

961   Pleistocene history of South America between 38 S and 56 S. Quaternary Science Reviews 27, 365–

962   390.

963   González-Acuña, J., Arroyo-Suarez, E., 2013. Comparative methodologies for sounding reduction

964   applied to a bathymetric survey referred to the WGS-84 ellipsoid. Executed in Concepcion Bay and

965   Gulf of Arauco, VIII Region, Chile., US Hydro 1.

966   Gordillo, S., Bujalesky, G.G., Pirazzoli, P.A., Rabassa, J.O., Saliège, J.-F., 1992. Holocene raised

967   beaches along the northern coast of the Beagle Channel, Tierra del Fuego, Argentina.

968   Palaeogeography, Palaeoclimatology, Palaeoecology 99, 41–54.

969   Hart, E.A., Stapor, F.W., Jerez, J.E.N., Sutherland, C.J., 2017. Progradation of a Beach Ridge Plain

970   between 5000 and 4000 Years BP Inferred from Luminescence Dating, Coquimbo Bay, Chile.

971   Journal of Coastal Research 33, 1065–1073.

972   Hervé, F., Ota, Y., 1993. Fast Holocene uplift rates at the Andes of Chiloé, southern Chile. Andean

973   Geology 20, 15–23.

974   Heusser, C.J., Flint, R.F., 1977. Quaternary glaciations and environments of northern Isla Chiloé,

975   Chile. Geology 5, 305–308.

976   Heusser, C.J., Streeter, S.S., 1980. A temperature and precipitation record of the past 16,000 years in

977   southern Chile. Science 210, 1345–1347.

978   Hijma, M.P., Engelhart, S.E., Törnqvist, T.E., Horton, B.P., Hu, P., Hill, D.F., 2015. A protocol for a

979   geological sea-level database. Handbook of Sea-Level Research, edited by: Shennan, I., Long, AJ,

980   and Horton, BP, Wiley Blackwell 536–553.

981   Hilleman, C., 2015. Upper-plate deformation following megathrust earthquakes: Holocene slip along

982   the El Yolki Fault in central Chile inferred from deformed coastal sediments. Masters Thesis,

983   University of Potsdam.

984   Hocking, E.P., Garrett, E., Cisternas, M., 2017. Modern diatom assemblages from Chilean tidal

985   marshes and their application for quantifying deformation during past great earthquakes. Journal

986   of Quaternary Science 32, 396–415.

987   Hogg, A.G., Hua, Q., Blackwell, P.G., Niu, M., Buck, C.E., Guilderson, T.P., Heaton, T.J., Palmer, J.G.,

988   Reimer, P.J., Reimer, R.W., 2013. SHCal13 Southern Hemisphere calibration, 0–50,000 years cal BP.

989   Radiocarbon 55, 1889–1903.

990   Hong, I., Dura, T., Ely, L.L., Horton, B.P., Nelson, A.R., Cisternas, M., Nikitina, D., Wesson, R.L., 2017. A

991   600-year-long stratigraphic record of tsunamis in south-central Chile. The Holocene 27, 39–51.

992   Horton, B.P., Shennan, I., 2009. Compaction of Holocene strata and the implications for relative

993   sealevel change on the east coast of England. Geology 37, 1083–1086.

994   Hua, Q., Barbetti, M., Rakowski, A.Z., 2013. Atmospheric radiocarbon for the period 1950–2010.

995   Radiocarbon 55, 2059–2072.

996   Hulton, N.R.J., Purves, R.S., McCulloch, R.D., Sugden, D.E., Bentley, M.J., 2002. The last glacial

997   maximum and deglaciation in southern South America. Quaternary Science Reviews 21, 233–241.

998   Ingram, B.L., Southon, J.R., 1996. Reservoir ages in eastern Pacific coastal and estuarine waters.

999   Radiocarbon 38, 573–582.

Isla, F.I., Flory, J.Q., Martínez, C., Fernández, A., Jaque, E., 2012. The evolution of the Bío Bío delta and the coastal plains of the Arauco Gulf, Bío Bío Region: the Holocene sea-level curve of Chile. Journal of Coastal Research 28, 102–111.

Isla, F.I., 1989. Holocene sea-level fluctuation in the southern hemisphere. Quaternary Science Reviews 8, 359–368.

Jara-Muñoz, J., Melnick, D., 2015. Unravelling sea-level variations and tectonic uplift in wave-built marine terraces, Santa María Island, Chile. Quaternary Research 83, 216–228.

Jara-Muñoz, J., Melnick, D., Brill, D., Strecker, M.R., 2015. Segmentation of the 2010 Maule Chile earthquake rupture from a joint analysis of uplifted marine terraces and seismic-cycle deformation patterns. Quaternary Science Reviews 113, 171–192.

Jara-Muñoz, J., Melnick, D., Zambrano, P., Rietbrock, A., González, J., Argandoña, B., Strecker, M.R., 2017. Quantifying offshore fore-arc deformation and splay-fault slip using drowned Pleistocene shorelines, Arauco Bay, Chile. Journal of Geophysical Research: Solid Earth 122, 4529–4558.

Kaizuka, S., Matsuda, T., Nogami, M., Yonekura, N., 1973. Quaternary tectonic and recent seismic crustal movements in the Arauco Peninsula and its environs, central Chile. Geographical Reports of Tokyo Metropolitan University 8, 1–49.

Khan, N.S., Ashe, E., Horton, B.P., Dutton, A., Kopp, R.E., Brocard, G., Engelhart, S.E., Hill, D.F., Peltier, W.R., Vane, C.H., 2017. Drivers of Holocene sea-level change in the Caribbean. Quaternary Science Reviews 155, 13–36.

Khan, N.S., Ashe, E., Shaw, T.A., Vacchi, M., Walker, J., Peltier, W.R., Kopp, R.E., Horton, B.P., 2015. Holocene relative sea-level changes from near-, intermediate-, and far-field locations. Current Climate Change Reports 1, 247–262.

Khan, N.S., Horton, B.P., Engelhart, S., Rovere, A., Vacchi, M., Ashe, E.L., Törnqvist, T.E., Dutton, A., Hijma, M.P., Shennan, I., 2019. Inception of a global atlas of sea levels since the Last Glacial Maximum. Quaternary Science Reviews 220, 359–371.

1025   Khazaradze, G., Wang, K., Klotz, J., Hu, Y., He, J., 2002. Prolonged post-seismic deformation of the

1026   1960 great Chile earthquake and implications for mantle rheology. Geophysical Research Letters

1027   29, 1–7.

1028   Klein, E., Vigny, C., Fleitout, L., Grandin, R., Jolivet, R., Rivera, E., Métois, M., 2017. A comprehensive

1029   analysis of the Illapel 2015 Mw8. 3 earthquake from GPS and InSAR data. Earth and Planetary

1030   Science Letters 469, 123–134.

1031   Lange, D., Cembrano, J., Rietbrock, A., Haberland, C., Dahm, T., Bataille, K., 2008. First seismic record

1032   for intra-arc strike-slip tectonics along the Liquiñe-Ofqui fault zone at the obliquely convergent

1033   plate margin of the southern Andes. Tectonophysics 455, 14–24.

1034   Lange, H., Casassa, G., Ivins, E.R., Schröder, L., Fritsche, M., Richter, A., Groh, A., Dietrich, R., 2014.

1035   Observed crustal uplift near the Southern Patagonian Icefield constrains improved viscoelastic

1036   Earth models. Geophysical Research Letters 41, 805–812.

1037   Leonard, E.M., Wehmiller, J.F., 1991. Geochronology of marine terraces at Caleta Michilla, northern

1038   Chile; implications for Late Pleistocene and Holocene uplift. Andean Geology 18, 81–86.

1039   Li, S., Bedford, J., Moreno, M., Barnhart, W.D., Rosenau, M., Oncken, O., 2018. Spatiotemporal

1040   variation of mantle viscosity and the presence of cratonic mantle inferred from 8 years of

1041   postseismic deformation following the 2010 Maule, Chile, earthquake. Geochemistry, Geophysics,

1042   Geosystems 19, 3272–3285.

1043   Lorenzo-Martín, F., Roth, F., Wang, R., 2006. Inversion for rheological parameters from post-seismic

1044   surface deformation associated with the 1960 Valdivia earthquake, Chile. Geophysical Journal

1045   International 164, 75–87.

1046   Marquardt, C., Lavenu, A., Ortlieb, L., Godoy, E., Comte, D., 2004. Coastal neotectonics in Southern

1047   Central Andes: uplift and deformation of marine terraces in Northern Chile (27 S). Tectonophysics

1048   394, 193–219.

1049   May, S.M., Zander, A., Francois, J.P., Kelletat, D., Pötsch, S., Rixhon, G., Brückner, H., 2015.

1050   Chronological and geoarchaeological investigations on an anthropogenic shell accumulation layer

1051   in the Longotoma dune field (Central Chile). Quaternary International 367, 32–41.

1052   May, S.M., Pint, A., Rixhon, G., Kelletat, D., Wennrich, V., Brückner, H., 2013. Holocene coastal

1053   stratigraphy, coastal changes and potential palaeoseismological implications inferred from geo-

1054   archives in Central Chile (29–32 S). Zeitschrift für Geomorphologie, Supplementary Issues 57, 201–

1055   228.

1056   McCulloch, R.D., Bentley, M.J., Purves, R.S., Hulton, N.R.J., Sugden, D.E., Clapperton, C.M., 2000.

1057   Climatic inferences from glacial and palaeoecological evidence at the last glacial termination,

1058   southern South America. Journal of Quaternary Science: Published for the Quaternary Research

1059   Association 15, 409–417.

1060   McCulloch, R.D., Davies, S.J., 2001. Late-glacial and Holocene palaeoenvironmental change in the

1061   central Strait of Magellan, southern Patagonia. Palaeogeography, Palaeoclimatology,

1062   Palaeoecology 173, 143–173.

1063   Melnick, D., 2016. Rise of the central Andean coast by earthquakes straddling the Moho. Nature

1064   Geoscience 9, 401.

1065   Melnick, D., Cisternas, M., Moreno, M., Norambuena, R., 2012. Estimating coseismic coastal uplift

1066   with an intertidal mussel: calibration for the 2010 Maule Chile earthquake (M w= 8.8). Quaternary

1067   Science Reviews 42, 29–42.

1068   Melnick, D., Hillemann, C., Jara-Muñoz, J., Garrett, E., Cortés-Aranda, J., Molina, D., Tassara, A.,

1069   Strecker, M.R., 2019. Hidden Holocene slip along the coastal El Yolki fault in Central Chile and its

1070   possible link with megathrust earthquakes. Journal of Geophysical Research: Solid Earth *124*.

1071   https://doi.org/10.1029/ 2018JB017188.

1072   Melnick, D., Li, S., Moreno, M., Cisternas, M., Jara-Muñoz, J., Wesson, R., Nelson, A., Báez, J.C., Deng,

1073   Z., 2018. Back to full interseismic plate locking decades after the giant 1960 Chile earthquake.

1074   Nature communications 9, 3527.

1075   Mercer, J.H., 1970. Variations of some Patagonian glaciers since the Late-Glacial; II. American Journal

1076   of Science 269, 1–25.

1077   Nelson, A.R., Kashima, K., Bradley, L.-A., 2009. Fragmentary evidence of great-earthquake

1078   subsidence during Holocene emergence, Valdivia Estuary, south central Chile. Bulletin of the

1079   Seismological Society of America 99, 71–86.

1080   Nelson, A.R., Manley, W.F., 1992. Holocene coseismic and aseismic uplift of Isla Mocha, south-

1081   central Chile. Quaternary International 15, 61–76.

1082   Orford, J.D., Carter, R.W.G., Jennings, S.C., 1991. Coarse clastic barrier environments: evolution and

1083   implications for Quaternary sea level interpretation. Quaternary International 9, 87–104.

1084   Ortlieb, L., Vargas, G., Saliège, J.-F., 2011. Marine radiocarbon reservoir effect along the northern

1085   Chile–southern Peru coast (14–24 S) throughout the Holocene. Quaternary Research 75, 91–103.

1086   Ota, Y., Paskoff, R., 1993. Holocene deposits on the coast of north-central Chile: radiocarbon ages

1087   and implications for coastal changes. Andean Geology 20, 25–32.

1088   Otvos, E.G., 2000. Beach ridges—definitions and significance. Geomorphology 32, 83–108.

1089   Peltier, W.R., 2004. Global glacial isostasy and the surface of the ice-age Earth: the ICE-5G (VM2)

1090   model and GRACE. Annual Reviews of Earth and Planetary Science 32, 111–149.

1091   Peltier, W.R., Argus, D.F., Drummond, R., 2015. Space geodesy constrains ice age terminal

1092   deglaciation: The global ICE-6G_C (VM5a) model. Journal of Geophysical Research: Solid Earth 120,

1093   450–487.

1094   Pico, T., Creveling, J.R., Mitrovica, J.X., 2017. Sea-level records from the US mid-Atlantic constrain

1095   Laurentide Ice Sheet extent during Marine Isotope Stage 3. Nature Communications 8, 1–6.

1096   Pino, M., Navarro, R.X., 2005. Geoarqueología del sitio arcaico Chan-Chan 18, costa de Valdivia:

1097   discriminación de ambientes de ocupación humana y su relación con la transgresión marina del

1098   Holoceno Medio. Revista geológica de Chile 32, 59–75.

1099   Pirazzoli, P.A., 1991. World atlas of Holocene sea-level changes. Elsevier.

1100   Plafker, G., Savage, J.C., 1970. Mechanism of the Chilean earthquakes of May 21 and 22, 1960.

1101   Geological Society of America Bulletin 81, 1001–1030.

1102   Porter, S.C., Stuiver, M., Heusser, C.J., 1984. Holocene sea-level changes along the Strait of Magellan

1103   and Beagle Channel, southernmost South America. Quaternary Research 22, 59–67.

1104   Rabassa, J., Clapperton, C.M., 1990. Quaternary glaciations of the southern Andes. Quaternary

1105   Science Reviews 9, 153–174.

1106   Rabassa, J., Heusser, C., Stuckenrath, R., 1986. New data on Holocene sea transgression in the

1107   Beagle Channel: Tierra del Fuego, Argentina, in: International Symposium on Sea-Level Changes

1108   and Quaternary Shorelines. pp. 291–309.

1109   Rehak, K., Strecker, M.R., Echtler, H.P., 2008. Morphotectonic segmentation of an active forearc, 37–

1110   41 S, Chile. Geomorphology 94, 98–116.

1111   Reimer, P.J., Bard, E., Bayliss, A., Beck, J.W., Blackwell, P.G., Bronk Ramsey, C., Buck, C.E., Cheng, H.,

1112   Edwards, R.L., Friedrich, M., 2013. IntCal13 and Marine13 radiocarbon age calibration curves 0-

1113   50,000 years cal BP. Radiocarbon 55, 1869–1887.

1114   Reyes, O., Méndez, C., San Román, M., Francois, J.-P., 2018. Earthquakes and coastal archaeology:

1115   Assessing shoreline shifts on the southernmost Pacific coast (Chonos Archipelago 43 50'–46 50' S,

1116   Chile, South America). Quaternary International 463, 161–175.

1117   Richter, A., Ivins, E., Lange, H., Mendoza, L., Schröder, L., Hormaechea, J.L., Casassa, G., Marderwald,

1118   E., Fritsche, M., Perdomo, R., 2016. Crustal deformation across the Southern Patagonian Icefield

1119   observed by GNSS. Earth and Planetary Science Letters 452, 206–215.

1120   Rignot, E., Rivera, A., Casassa, G., 2003. Contribution of the Patagonia Icefields of South America to

1121   sea level rise. Science 302, 434–437.

1122   Rosenau, M., Melnick, D., Echtler, H., 2006. Kinematic constraints on intra-arc shear and strain

1123   partitioning in the southern Andes between 38 S and 42 S latitude. Tectonics 25.

1124   Schellmann, G., Radtke, U., 2010. Timing and magnitude of Holocene sea-level changes along the

1125   middle and south Patagonian Atlantic coast derived from beach ridge systems, littoral terraces and

1126   valley-mouth terraces. Earth-Science Reviews 103, 1–30.

1127   Shennan, I., 2015. Framing research questions, in: Shennan, I., Long, A.J., Horton, B.P. (Eds.),

1128   Handbook of Sea-Level Research. John Wiley & Sons, pp. 3–25.

1129   Shennan, I., Bradley, S.L., Edwards, R., 2018. Relative sea-level changes and crustal movements in

1130   Britain and Ireland since the Last Glacial Maximum. Quaternary Science Reviews 188, 143–159.

1131   Shennan, I., Milne, G., Bradley, S., 2012. Late Holocene vertical land motion and relative sea-level

1132   changes: lessons from the British Isles. Journal of Quaternary Science 27, 64–70.

1133   Shennan, I., Peltier, W.R., Drummond, R., Horton, B., 2002. Global to local scale parameters

1134   determining relative sea-level changes and the post-glacial isostatic adjustment of Great Britain.

1135   Quaternary Science Reviews 21, 397–408.

1136   Stefer, S., Moernaut, J., Melnick, D., Echtler, H.P., Arz, H.W., Lamy, F., De Batist, M., Oncken, O.,

1137   Haug, G.H., 2010. Forearc uplift rates deduced from sediment cores of two coastal lakes in south-

1138   central Chile. Tectonophysics 495, 129–143.

1139   Tamura, T., 2012. Beach ridges and prograded beach deposits as palaeoenvironment records. Earth-

1140   Science Reviews 114, 279–297.

1141   Taylor, R.E., Berger, R., 1967. Radiocarbon content of marine shells from the Pacific coasts of Central

1142   and South America. Science 158, 1180–1182.

1143   Vacchi, M., Marriner, N., Morhange, C., Spada, G., Fontana, A., Rovere, A., 2016. Multiproxy

1144   assessment of Holocene relative sea-level changes in the western Mediterranean: sea-level

1145   variability and improvements in the definition of the isostatic signal. Earth-Science Reviews 155,

1146   172–197.

1147   Vacchi, M., Engelhart, S.E., Nikitina, D., Ashe, E.L., Peltier, W.R., Roy, K., Kopp, R.E., Horton, B.P.,

1148   2018. Postglacial relative sea-level histories along the eastern Canadian coastline. Quaternary

1149   Science Reviews 201, 124–146.

1150 Van de Plassche, O., 1986. Sea-level research: A manual for the collection and evaluation of data:

1151   Norwich. UK, Geobooks.

1152 Villa-Martínez, R., Villagrán, C., 1997. Historia de la vegetación de bosques pantanosos de la costa de

1153   Chile central durante el Holoceno medio y tardío. Revista Chilena de Historia Natural 70, 391–401.

1154 Villalobos Silva, M.P., 2005. Evidencias de la fluctuación del nivel del mar y alzamientos tectónicos

1155   desde el Pleistoceno tardío en isla Mancera X Región de Los Lagos-Chile: registro estratigráfico y

1156   sedimentológico. Doctoral Thesis, Universidad Austral de Chile.

1157 Von Huene, R., Kulm, L.D., Miller, J., 1985. Structure of the frontal part of the Andean convergent

1158   margin. Journal of Geophysical Research: Solid Earth 90, 5429–5442.

1159 Wesson, R.L., Cisternas, M., Ely, L.L., Melnick, D., Briggs, R.W., Garrett, E., 2014. Uncertainties in field

1160   estimation of mean sea level, in: Barlow, N.L.M., Koehler, R. (Eds.), Seismic and Non-Seismic

1161   Influences on Coastal Change in Alaska. Alaska Division of Geological and Geophysical Surveys

1162   Guidebook, p. 165pp.

1163 Willis, M.J., Melkonian, A.K., Pritchard, M.E., Rivera, A., 2012. Ice loss from the Southern Patagonian

1164   ice field, South America, between 2000 and 2012. Geophysical Research Letters 39, L17501.

1165 Wiseman, K., Bürgmann, R., Freed, A.M., Banerjee, P., 2015. Viscoelastic relaxation in a

1166   heterogeneous Earth following the 2004 Sumatra–Andaman earthquake. Earth and Planetary

1167   Science Letters 431, 308–317.

1168 Xu, W., 2017. Finite-fault Slip Model of the 2016 Mw 7.5 Chiloé Earthquake, Southern Chile,

1169   Estimated from Sentinel-1 Data. Geophysical Research Letters 44, 4774–4780.